FRACTURE TOUGHNESS OF CALCIA PARTIALLY-STABILISED ZIRCONIA

FRACTURE TOUGHNESS OF CALCIA PARTIALLY-STABILISED ZIRCONIA

by

DAVID JOHN GREEN, B.Sc.

A Thesis

Submitted to the School of Graduate Studies

in Partial Fulfillment of the Requirements

for the Degree

Master of Science

McMaster University

September, 1972

MASTER OF SCIENCE
(Metallurgy and Materials Science)

McMASTER UNIVERSITY
Hamilton, Ontario

TITLE: Fracture Toughness of Calcia Partially-Stabilised Zirconia

AUTHOR: David John Green, B.Sc. (University of Liverpool, England)

SUPERVISOR: Dr. P. S. Nicholson

NUMBER OF PAGES: xii, 122.

ABSTRACT

The room-temperature fracture behaviour of calcia partially-stabilised zirconia (PSZ) was investigated. Fracture energy measurements were made using the standard stress intensity calibration and work to fracture techniques. The detailed nature of the PSZ microstructure was studied using scanning electron microscopy, qualitative X-ray analysis and T.E.M. surface replication. The grain structure was determined to be bimodal with small grains of pure zirconia dispersed along the boundaries of larger grains. These large grains consist of a binary pure-zirconia/stabilised zirconia mixture. An attempt was made to relate the fracture properties to the nature of the inherent flaws present in the material.

The strength of calcia partially-stabilised zirconia was observed to depend on the size and distribution of the grain boundary precipitate of pure zirconia. It is postulated that this grain boundary precipitate causes decohesion and weakening of some of the grain boundaries due to the large internal stresses associated with its martensitic phase transformation. This phenomena of grain boundary decohesion leads to elastic non-linearity and hysteresis. Crack propagation was always observed to proceed in a slow controlled fashion in this material. A model is proposed to explain these observations based on the formation of a microcrack zone at the tip of a propagating crack. The occurrence of continued stable crack propagation is believed associated with increasing microcrack zone size with increasing crack length. Evidence supporting this model is presented.

ACKNOWLEDGMENTS

The author wishes to express his gratitude to those members of the Department of Metallurgy and Materials Science who assisted in this work. Sincere thanks are due to Dr. P. S. Nicholson for his advice and supervision and to Dr. J. D. Embury for his criticism and interest in the development of the program.

Special thanks are due to Miss L. de Jong for her careful handling and typing of the thesis; to Mr. D. Hodgson for his careful work on the drawings, ; to Mr. T. Bryner for his work on the photographs and to Mr. M. VanOosten for his solution to the chemical analysis.

The author is also grateful to Mr. J. Van den Andel of Westinghouse (Canada) Ltd., for his precise help in the ultrasonic elastic modulus determination, to Mr. M. Tracz of Indusmin Ltd. for his help in the dilatometry, and to Dr. A. Heuer for his electron micrographs.

The interest and financial support of the Atomic Energy of Canada Limited is gratefully acknowledged.

Finally, the author is indebted to the other members of the ceramic group and to all those people who have made my introduction to Canada more than academic.

TABLE OF CONTENTS

LIST OF TABLES

LIST OF ILLUSTRATIONS

TO MY MOTHER

CHAPTER I

LITERATURE REVIEW AND THEORY

I.1 Introduction

In order for ceramics to be used in structural or engineering applications, they must compete in terms of mechanical properties and cost. The most serious drawback of ceramics is their proneness to catastrophic failure, particularly under conditions of mechanical and thermal shock. This inherent brittleness has led to the use of ceramics in applications where their special properties of hardness, chemical inertness, low thermal and electrical conductivities and temperature stability are important.

Recent developments have shown that ceramics of strengths approaching 100,000 psi can be fabricated. These advances have occurred largely by the empirical observation that increased strength can be brought about by the elimination of pores and the refinement of grain size [1-3]. In these developments, very little use has been made of a basic understanding of the fracture process and its microstructural dependence.

Fortunately, techniques [4, 5] are now available to measure the relative resistance to crack propagation and it should be possible to obtain a detailed insight into the mechanisms of crack propagation

and its correlation to structure.

Recent studies [6] on calcia partially-stabilised zirconia have shown this material to have good thermal shock resistance. It was therefore decided to determine if this thermal shock resistance implied a degree of fracture toughness and a study of crack propagation in the material was undertaken.

1.2 Fracture of Brittle Materials

1.2.1 Strength of Ceramics

Ceramics are inorganic, non-metallic glasses or crystalline solids, frequently with non-equilibrium microstructures. The tendency to fail by cleavage rather than shear is an inherent feature of their structure.

Ceramic materials are bound by strongly polarised, ionic bonds, covalent bonds, or some intermediate covalent-ionic bonds. The directionality of this type of bonding gives ceramics high Young's moduli and low densities. The crystals, therefore, tend to have planes of low surface energy, high melting points, low coefficients of thermal expansion and low electrical and thermal conductivities.

In theoretical considerations on the nature of crystals one must consider the role of the defects present and in the study of strength the role of dislocations and cracks are most important.

The ductility of polycrystalline ceramics tends to be very limited at ambient temperatures since the stress level to move mobile dislocations is high and there are generally insufficient slip systems [7,8] to allow a homogeneous strain to occur by slip.

The occurrence of limited slip can be very harmful to the strength of ceramics since stress concentrations at blocked slip bands and twin interactions, near a crack or simply at elastic inhomogeneities, cannot be relieved. This inability to relax such stress concentrations makes these materials sensitive to damage. It is most important, therefore, to carefully examine and prepare external surfaces before ceramics are mechanically tested. In studies of semi-brittle solids, such as rock salt and magnesia, the problem of anisotropic plastic flow and its accommodation problems appear to play an important role in the initiation, growth and propagation of cracks [9].

The effect of plastic deformation will, however, be assumed to be negligible except on a microscopic scale in the rest of this discussion. Mechanical failure will be explained by the presence and propagation of pre-existing flaws. This neglect of plastic deformation limits the discussion to the relevance of the thesis topic and observations but, in general, even the limited plasticity at ambient temperatures can influence the brittle fracture of ceramics.

Cracks may be formed internally if surface energy relationships do not favour cohesion and methods of fabrication, such as sintering, can lead to deleterious porosity or internal stress production. For instance, when ceramic bodies are cooled to room temperature following firing, internal stresses may develop due to phase transformations or

anisotropic thermal contractions. Crack nucleation due to anisotropic thermal contraction has been treated by Clarke [10] and has been demonstrated by Davidge and Tappin [11] on polycrystalline beryllia. It is important to note, however, that internal stresses have been purposely generated to strengthen materials. This generally consists of surface compressive stresses introduced by glazing [12], chemical [13] or thermal [14] treatments. These internal stresses are particularly important in two-phase ceramics, wherein differences in thermal expansion coefficients or elastic constants of the two phases can lead to stress concentrations and the possible formation of cracks or weak interfaces. The stresses due to thermal expansion differences have been treated by Selsing [15] and by Hasselman and Fulrath [16], who considered elastic constant differences. Other factors which influence the strength of two-phase systems are the size and volume fraction of the second phase [16,17].

In general, fracture is initiated in these materials by the extension of inherent flaws or by local anisotropic deformation. The general trend with temperature and the importance of these two mechanisms is shown in Figure 1. At very high temperatures secondary slip may occur at sufficiently low stresses to prevent crack initiation or propagation at the flow stress. Gross plastic deformation of the material will then precede fracture. The extent of these regions of different fracture behaviour will vary considerably from one brittle material to the next and these variations in ceramic behaviour have been discussed by Davidge and Evans [18].

The above discussion does not imply that the toughness of ceramics cannot be improved. If secondary slip can be induced by second-phase

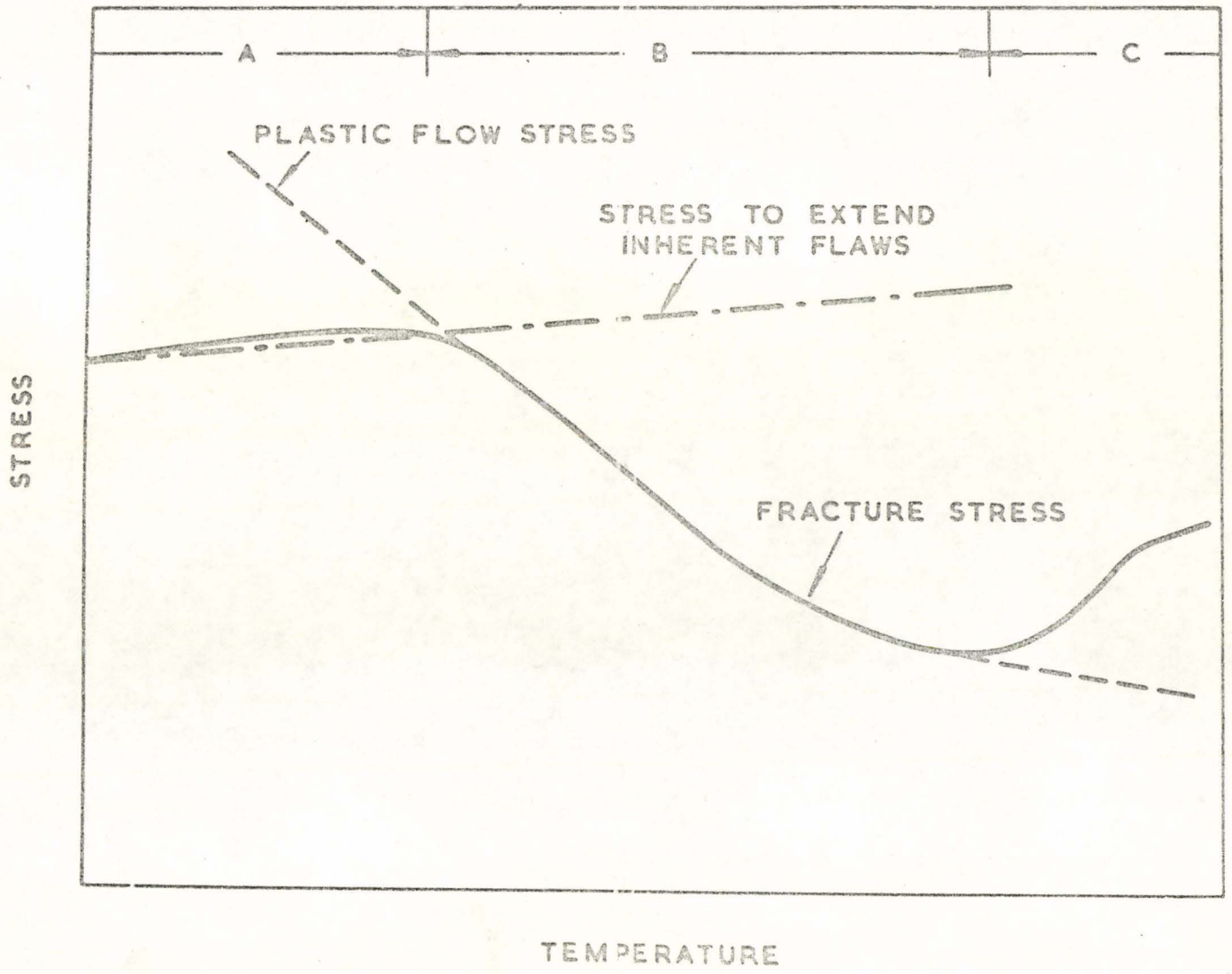

Figure 1. Fracture Behaviour of Ceramics as a Function of Temperature, After Davidge and Evans [18].

particles, the ductility of the material could be extended. This, however, has not been observed yet in two-phase ceramics. The other route is to avoid plastic flow altogether and generate resistance to crack propagation by the "deflection" of moving cracks in two-phase or fibrous microstructures.

In two-phase, precipitation-strengthened ceramics, crack-particle interactions constitute the main resistance to crack propagation. These interactions can take several forms; that is, the elastic interaction of the precipitate with the matrix may lead to perturbation of stress fields in the vicinity of the particle and so deflect the propagating crack. Failure of the matrix-particle interface under the influence of the stress-field of the crack has been discussed by Cook and Gordon [19] for the case of tensile failure of interfaces perpendicular to the plane of the crack and by Kelly [20] for the case of interfacial shear. Both these mechanisms would lead to effective crack blunting and an increase, therefore, in the resistance to crack propagation. Precipitate particles, which fail by ductile rupture rather than cleavage could also absorb some of the crack energy and thereby enhance the toughness of such two-phase materials. There have been several recent advances in the precipitation-strengthening of ceramics and these have been reviewed by Groves [21]. More recently, Chyung et al. [22] reported increased toughness in glass-ceramics, in which mica was internally nucleated and crystallised as a precipitate in the glass. Fibre-reinforced ceramics could also produce similar mechanisms of toughness, though advances here have been mainly restricted to ceramic fibre-metal or ceramic fibre-polymer composite technology.

1.2.2 Flaw Theory of Fracture

At an atomistic level, the fracture strength of a material depends on the physical and chemical forces holding it together. The cohesive strength of a material provides a means of comparing the potential strengths of different materials and gives the maximum strength that can be expected for a given material.

There are various methods to calculate this theoretical strength [23], depending on how the potential is chosen to describe the separation force between two planes of atoms. All these approaches yield approximately the same answer with the theoretical tensile stress being E/10 where E is the Young's modulus of the material [23]. These theoretical strengths have been observed in some single crystal fibres and whiskers but for most engineering materials, the theoretical strength is two orders of magnitude too large. The reason for this discrepancy in brittle materials is due to the presence of flaws.

The flaw theory of fracture originated with a crack propagation concept advanced by Griffith [24,25] who pointed out that an existing crack will propagate, if the available elastic strain energy release rate exceeds the increase in system surface energy accompanying the crack growth. That is, instead of separation of two planes of atoms as modelled for the theoretical strength, fracture will occur by "gradual" separation of atoms as an inherent crack increases in size. This theory yields the correct functional relationship between stress at fracture and flaw size as evidenced by many results on brittle materials [26,27].

It also predicts a theoretical cohesive strength of the correct order of magnitude as verified by single crystal whiskers [28].

Griffith suggested that the strength in tension of a brittle material is greatly affected by the presence of small cracks and other discontinuities within it. These cracks may be present before any load is applied or may be formed during application of the load. Fracture results from the high tensile stress concentrations induced at or near the crack tip as the material is loaded.

Griffith approached the problem in two ways which typify the modern approach of continuum fracture mechanics. He first investigated the elastic stress distribution using the stress analysis of Inglis [29], who showed that the tensile stress at the tip of a crack (length 2a) was:

$$\sigma_{yy} \cong 2\sigma \sqrt{a/\rho} \tag{1.1}$$

where σ_{yy} is the concentrated stress, σ the applied stress, and ρ the radius of the crack tip. The difficulty in evaluating the crack tip radius makes this approach difficult to resolve.

The second approach was based on a mechanical energy balance to determine the condition for material fracture. Griffith calculated the decrease in the elastic strain energy (U), in a plate of unit thickness, when a flat elliptic crack of length 2a is formed by an applied tensile stress σ, to be:

$$U = \frac{\pi a^2 \sigma^2}{E} \tag{1.2}$$

The total energy (W) of the newly formed crack surface will be:

$$W = 4a\gamma_o \tag{1.3}$$

where γ_o is the thermodynamic surface energy. Crack propagation will occur when the release of strain energy is at least equal to the rate of increase in free surface energy due to the formation of new surface area, i.e.,

$$\frac{\partial U}{\partial a} = \frac{\partial W}{\partial a} \tag{1.4}$$

When this relationship is substituted into equations (1.2) and (1.3) the fracture stress is given by:

$$\sigma_F = \sqrt{2E\gamma_o/\pi a} \tag{1.5}$$

This relationship in the form $\sigma_F \sqrt{a}$ = constant, has been shown to hold for many brittle and semi-brittle materials. Both these approaches are consistent and although the energy approach seems limited to two-dimensional cracks and ignores the cohesive forces which must be acting at the crack tip, it has been shown to apply in basically the same form to different three-dimensional crack geometries [30]. Griffith recognised the fact that forces must act at the crack tip but avoided their discussion by assuming a finite radius of curvature at the tip. This theory may seem an unnecessary oversimplification of a series of complicated phenomena, yet this simplicity has been responsible for the recent progress in design against brittle failure. Continuum fracture mechanics tends to emphasise engineering

usefulness rather than scientific and philosophical accuracy, while material science attempts to fill this conceptual void.

The relative merits of these two approaches have been discussed [31]. The stress concentration method assumes that a maximum stress must be surpassed for fracture to occur whilst the energy balance method assumes fracture occurs after creation of a maximum amount of stored energy. The two approaches are equivalent for cracks with a radius of curvature of the order of a few atomic spacings. For cracks with larger radii of curvature the stress concentration approach is more fundamental since it always presents a criteria for fracture in terms of the maximum cohesive strength. This fundamental approach is not very useful since the crack root radius cannot be easily evaluated and stress concentration calibration tends to be carried out for the case of sharp cracks where the two approaches are equivalent. In contrast, the energy approach establishes a criterion which reflects the irreversible processes at the crack tip, irrespective of its radius.

A generalised Griffith equation for any crack geometry can now be written:

$$\sigma_f = \frac{1}{Y} \sqrt{\frac{2E\gamma_I}{a}} \qquad (1.6)$$

where Y is a geometric factor associated with the test and specimen geometry and γ_I is the "effective" surface energy. The effective surface energy will therefore include terms other than the thermodynamic surface energy which is needed to create a planar fracture surface. These other terms consist of the effect of the other irreversible energy processes

which occur in crack propagation, such as plastic deformation or secondary crack formation.

The statement that fracture occurs when the stress condition in a sufficiently large volume exceeds a critical value may be readily converted to a mathematical model. The most general form for the stress distribution at the crack tip was given by Irwin [32,33], who noted that the stress field at any point near the crack tip, shown schematically in Figure 2, is related to the distance r from the crack tip, the angle of inclination θ and a constant K called the stress intensity factor. The radial dependence is always inversely proportional to the square root of the distance from the crack tip, regardless of type of loading, crack geometry or magnitude of the load.

Stress fields near a crack tip can be related to the three basic modes of deformation (Figure 3). Since ceramics generally fail in tension, mode I is of greatest importance, but superposition of these three modes is sufficient to describe the most general type of crack tip deformation in a general stress field. The stress field equations for mode I loading are listed below for the case of plane-strain deformation [30]:

$$\sigma_{xx} = [K_I/(2\pi r)^{1/2}] \cos \theta/2 \, [1-\sin \theta/2 \sin 3\theta/2] \tag{1.7}$$

$$\sigma_{yy} = [K_I/(2\pi r)^{1/2}] \cos \theta/2 \, [1+\sin \theta/2 \sin 3\theta/2] \tag{1.8}$$

$$\sigma_{xy} = [K_I/(2\pi r)^{1/2}] \sin \theta/2 \cos \theta/2 \cos 3\theta/2 \tag{1.9}$$

$$\sigma_{zz} = \nu (\sigma_{xx} + \sigma_{yy}), \; \sigma_{xz} = \sigma_{yz} = 0 \tag{1.10}$$

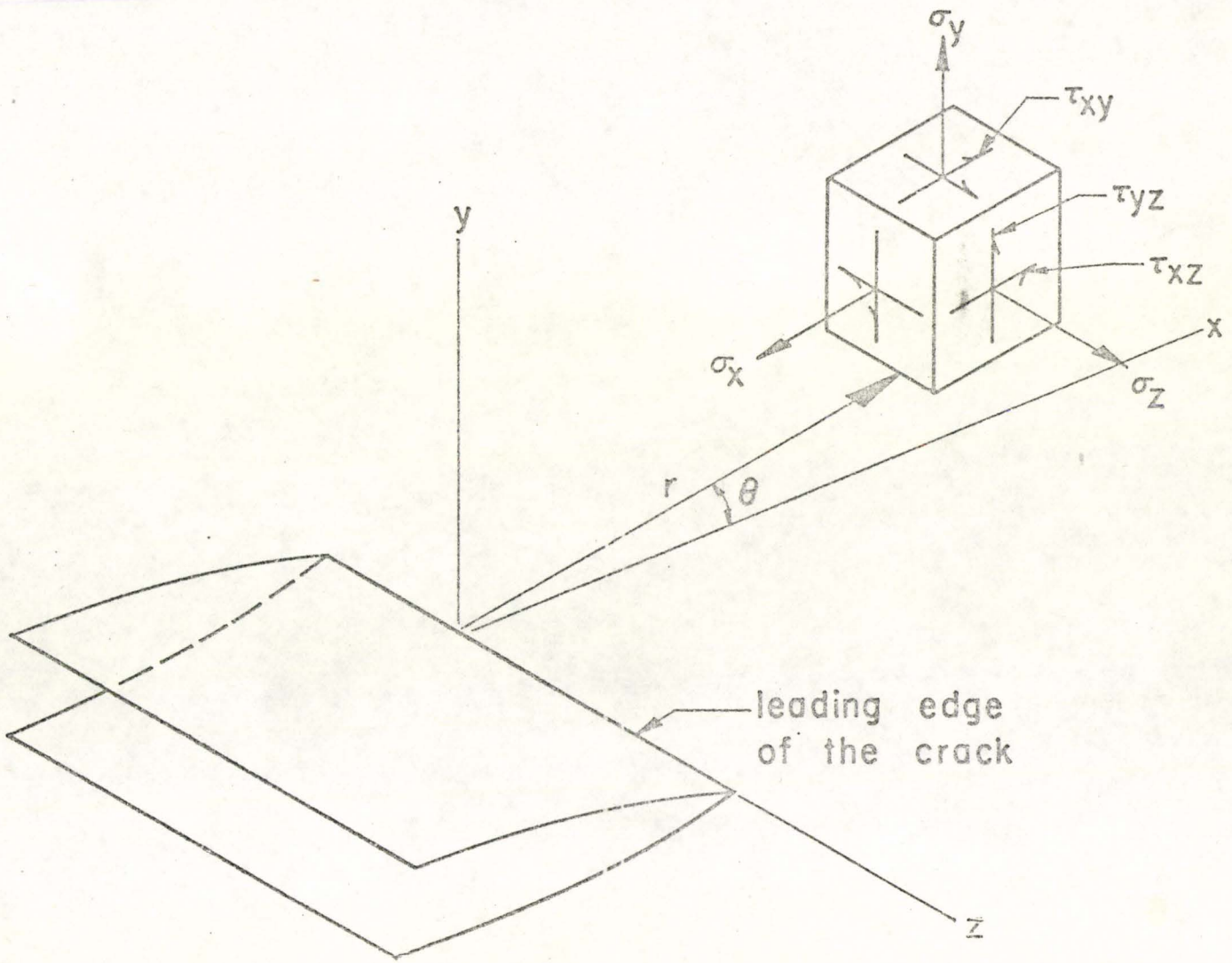

Figure 2. Co-ordinates Measured from the Leading Edge of a Crack and the Stress Components in the Crack Tip Stress Field. After Paris and Sih [30].

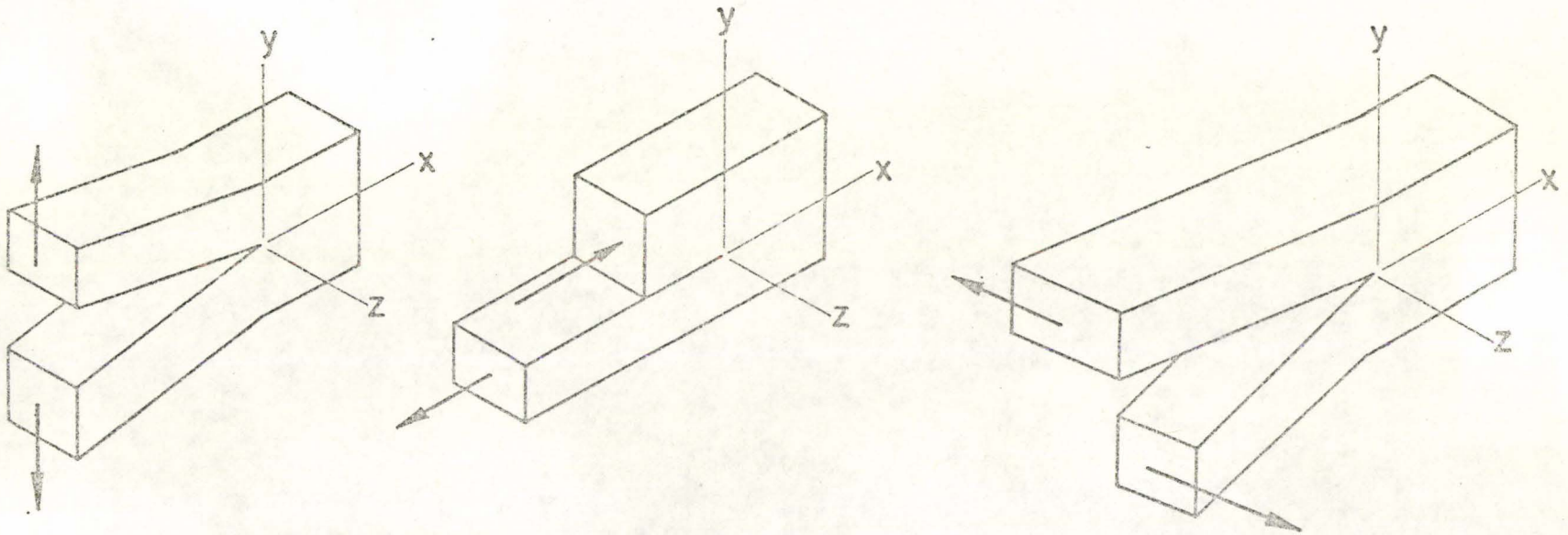

Figure 3. The Basic Modes of Crack Surface Displacement. After Paris and Sih [30].

where K_I is the stress intensity for mode I loading. The mathematics of these solutions involves the use of the complex variable to solve the bi-harmonic, equilibrium and elasticity equations and a simplified approach has been outlined by Eshelby [34]. Crack problems have now been solved for many test geometries [4,35] and all have the form:

$$K = Y\sigma(a)^{1/2} \qquad (1.11)$$

where Y is a constant, which depends on the test geometry. When a critical stress level is reached, denoted by K_C, fracture will occur. The concept of a critical stress intensity is the basis of the fracture toughness approach for evaluating materials.

In the stress intensity approach, no use has been made of an energy balance and mathematics cannot solve the difficulty since it must still be shown that the elastic stress distribution, with a singularity at the crack tip, describes the actual stress field with reasonable accuracy. In ductile materials, this can be a problem but adjustment of the specimen geometry or correction procedures can usually account for plastic zone effects. In the testing of ceramics at room temperature, there will generally be little plastic relaxation and this method can therefore be adequately applied. There exists, however, in ceramics the possibility of a microcrack zone at crack tips, which can act in a similar way to a plastic zone.

As mentioned previously the stress and energy approaches are equivalent and are easily related. In most ceramic literature the energy values of fracture toughness tend to be quoted, since it is hoped that the surface energy can be related to the energy absorbing

mechanisms at the crack tip. In metals this approach is difficult since the effective surface energy is affected by environment and plasticity in a complicated fashion.

In order to retain the usefulness of sharp crack fracture mechanics, the critical stress intensity must be defined in terms of the load and crack length at which the first significant crack growth takes place. Individual microscopic fractures must be expected due to the inhomogeneous nature of materials but a higher critical stress intensity may be more realistic and economical.

A most important aspect of fracture is the prediction of the geometric size effect. For brittle inhomogeneous materials there may be a statistical size effect which is superimposed on the geometric effect. The strength of brittle materials increases as the specimen size decreases while, for a given size, the strength measured in bending is greater than that measured in uniaxial tension. Statistical models of strength [36-38] are generally used to account for these effects and Weiss and Shaeffer [39] have shown that for inhomogeneous materials sharp crack fracture mechanics may not be able to account for the statistical size effect. As the volume subjected to the critical stress increases so does the chance of finding a severe inhomogeneity. The applicability of this idea is most important in ceramics and although it is not well clarified, experimental scatter may well indicate whether such a problem may develop.

As envisioned by Griffith, the work associated with the creation of new surfaces should be the thermodynamic surface energy. In most cases, however, the energy associated with a fracture is much greater

than the surface free energy. Irwin [40] and Orowan [26,31] first noted that the surface energy should be modified by a plastic work term, which in metals would be of prime importance. Even in ceramics, the "effective surface energy γ_I" is an order of magnitude greater than the thermodynamic surface energy and consists of a number of additional terms, reflecting the irreversible energy processes at the crack tip.

A general relationship between the effective surface energy and experimental parameters can be derived using a mechanical energy balance [40,27]. Consider a crack in a solid, subjected to a constant load P as shown in Figure 4. As the crack extends, the work dW, performed on the solid by the external load must equal the change of internal strain energy, dV, plus the change of surface energy, dS:

$$dW = dV + dS \tag{I.12}$$

The work done by the external load is Pdu, du being the differential displacement of the load as the crack extends a small amount. The total elastic strain energy of the body is:

$$V = \int Pdu \tag{I.13}$$

For a linear elastic body, the displacement is proportional to the applied load:

$$u = \lambda P \tag{I.14}$$

where λ is called the compliance of the system. It therefore follows that the total elastic energy is:

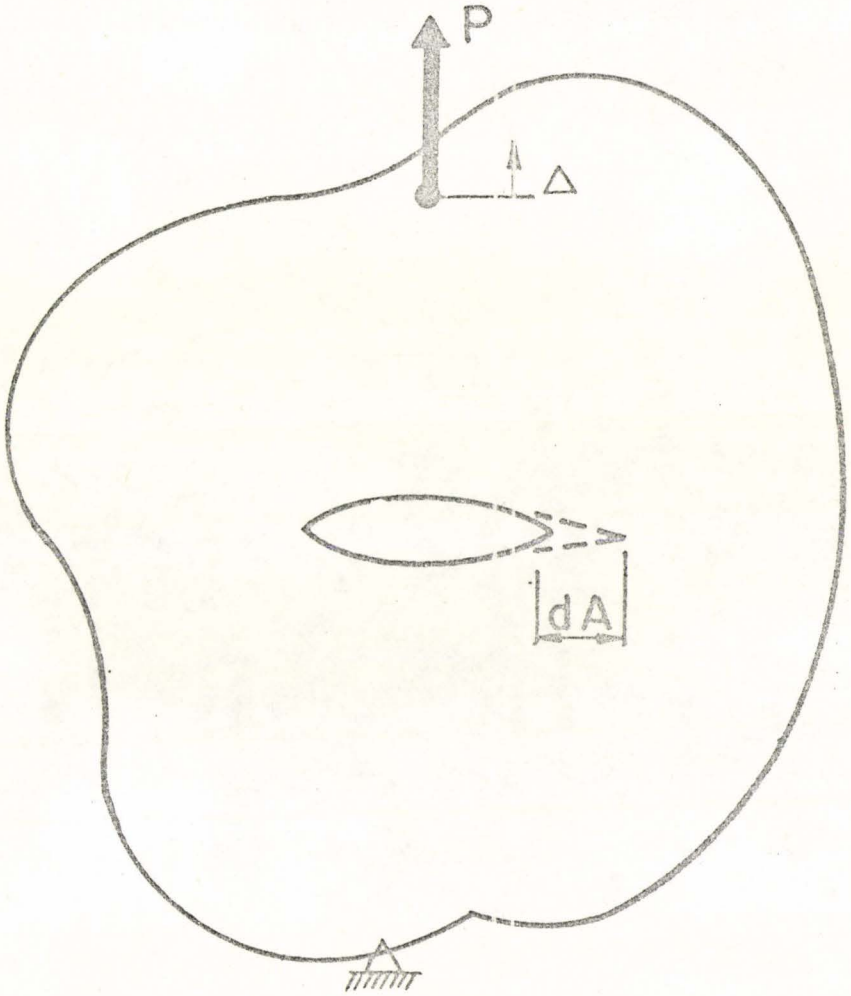

Figure 4. A Crack in a Body of Arbitrary Shape Subjected to a Load. After Paris and Sih [30].

$$V = u^2/2\lambda = Pu/2 \tag{1.15}$$

and at constant load:

$$dV = 1/2\ Pdu = 1/2\ dW \tag{1.16}$$

The change in effective surface energy is $2\gamma_I dA$ where $2dA$ is the amount of surface formed as the crack propagates a small amount. Substituting the expressions for dW, dV and dS into the energy balance, the following is obtained:

$$\gamma_I = (P^2/4)(\partial\lambda/\partial A)_P \tag{1.17}$$

which provides an experimental means of measuring γ_I.

Irwin originally expressed his results in terms of a strain energy release rate G which is just equal to twice the effective surface energy. In a similar way to the stress intensity factors, G_{IC}, G_{IIC} and G_{IIIC} represent the critical strain energy release rates for crack motion for modes I, II and III, respectively. The above derivation is also valid for constant strain as well as fixed-load conditions. For combined mode failure:

$$G = 2\gamma_I = G_I + G_{II} + G_{III}$$

which constitutes a generalised Griffith condition for crack propagation.

The relationship between the effective surface energy and stress intensity approaches to fracture can be easily proven [27,32,40]

and as a result these two fracture viewpoints can be used interchangeably. The relationship for plane strain with mode I loading is:

$$K_{IC}^2 = EG_{IC} \tag{1.18}$$

or

$$K_{IC}^2 = 2E\gamma_I \tag{1.19}$$

Originally a term $(1-\nu^2)$ was also included but it has been recommended recently [4] that this term should be neglected since it is not fully understood and its omission only leads to a small, conservative modification to the fracture criteria.

1.2.3 Modifications to the Fracture Surface Energy

Since the flaw theory was originally devised for homogeneous, isotropic solids, it should be modified whenever these conditions are not satisfied. The fact that solids are complex aggregates of grains, grain boundaries, inclusions and other inhomogeneities, fracture mechanics should be applied with caution.

In crystalline materials, the effective surface energy even in single crystals will depend on the orientation of the crack to the crystallographic axes of the solid [41]. This effect, however, tends to be averaged out in polycrystalline materials unless there is some material texture.

In many ceramics, grain boundaries tend to be weak because of the covalent nature of these solids. Fracture often occurs along grain boundaries and has been analysed thoroughly by Gilman [23,42]. In higher

strength ceramics, however, cleavage fracture seems to predominate. In this case, the available elastic energy is probably enough to overcome any energy barrier to this cleavage fracture which creates the least amount of surface area [43].

If crack propagation is hindered by obstacles such as grain boundaries and then re-initiates in a new direction an increase in the effective surface energy will be produced [44]. This apparent increase will depend on the angle of tilt or twist of the direction change. For intergranular failure, tilt propagation is most important and if it is assumed that the polycrystalline material is an aggregate of truncated octahedra, the angle of tilt will be 60° [45]. In real materials, the angle of tilt will scatter around this value, with angles in the range 60° to 90° being most important in the fracture process. Tilt angles in this range will increase the surface energy by a factor of 1.8 - 4.0 [46]. Crack branching phenomena are also associated with high speed crack propagation which causes re-distribution of the elastic stresses [47].

Probably the most complicating factor in fracture mechanics is the effect of plastic deformation. Since the aim of fracture mechanics is generally to predict the brittle strength of a material, it is necessary that errors introduced by plastic deformation be negligible or adequately corrected for. The size of the plastic zone will be affected by such factors as the specimen geometry and the state of stress at the crack tip. In ceramics at ambient temperatures, plastic deformation tends to be almost negligible but inclusion of a plastic work term is still important in most cases.

Other inhomogeneities such as pores, inclusions and microcracks will also cause local variations in the stress field at the crack tip and will therefore affect crack propagation. The production of microcracks, for instance, is of special interest in rock and concrete fracture mechanics [48,49], where such a zone can drastically alter the fracture characteristics of the material. The effects of microcracks on the mechanical properties of rocks has been thoroughly treated by Cook and Jaeger [49]. The influence of voids, in the form of cracks, very flat open cracks, and closed cracks, on the elastic properties of a body is most easily studied with the aid of the reciprocal theorem. This theorem states that for a body acted upon separately by two sets of applied stresses, the work done by the first set acting over the displacements produced by the second set equals the work done by the second set acting over the displacements produced by the first set. For example, it can be shown that [50] the effective Young's modulus of a body containing a large number of randomly oriented closed cracks of average length L per unit volume is:

$$E_{eff} = E_o/\{1+ \frac{2\pi L}{15} \left[\frac{2 + 3\mu^2 + 2\mu^4}{(1 + \mu^2)^{2/3}} - 2\mu \right] \} \qquad (1.20)$$

where μ is the coefficient of sliding friction between crack surfaces. This can be used to show that the initial Young's modulus for unloading a body containing a closed crack is equal to the intrinsic Young's modulus of the material, E_o.

It is interesting to study the distribution and dissipation of energy in a body containing a closed crack during compressive loading and

unloading. The stress-strain curve for this case is shown in Figure 5(a). The loading part is linear with an effective Young's modulus which is lower than the intrinsic modulus of the material due to the presence of the closed cracks. As the material is unloaded, the slope of the curve changes to the intrinsic modulus of the material, E_o. At a lower unloading stress reverse sliding of the crack surfaces commences and the unloading modulus decreases to a value even lower than the original effective Young's modulus. The area between the loading and unloading lines represents the work done against friction between the crack surfaces. Figure 5(b) shows the stress-strain curve for brittle materials containing voids, open cracks and closed cracks of different and often random orientations. The initial slope of the stress-strain curve on unloading provides a measure of the intrinsic Young's modulus of the material unless open voids are still present. Furthermore, the strain at zero load provides an indication of the amount of inherent compressive stress across crack surfaces in the material. Thus the form of the stress-strain curve for brittle materials, the observed hysteresis and the difference between static and dynamic moduli can be explained in terms of phenomena associated with the existence of cracks and cavities.

Another interesting effect of microcracks is their influence on the stability of crack propagation. The effective Young's modulus for a material containing a Griffith crack is given by [51]:

$$E_{eff} = E_o / (1 + 2\pi La^2) \qquad (1.21)$$

which, when substituted in the Griffith equation (1.5) gives the locus

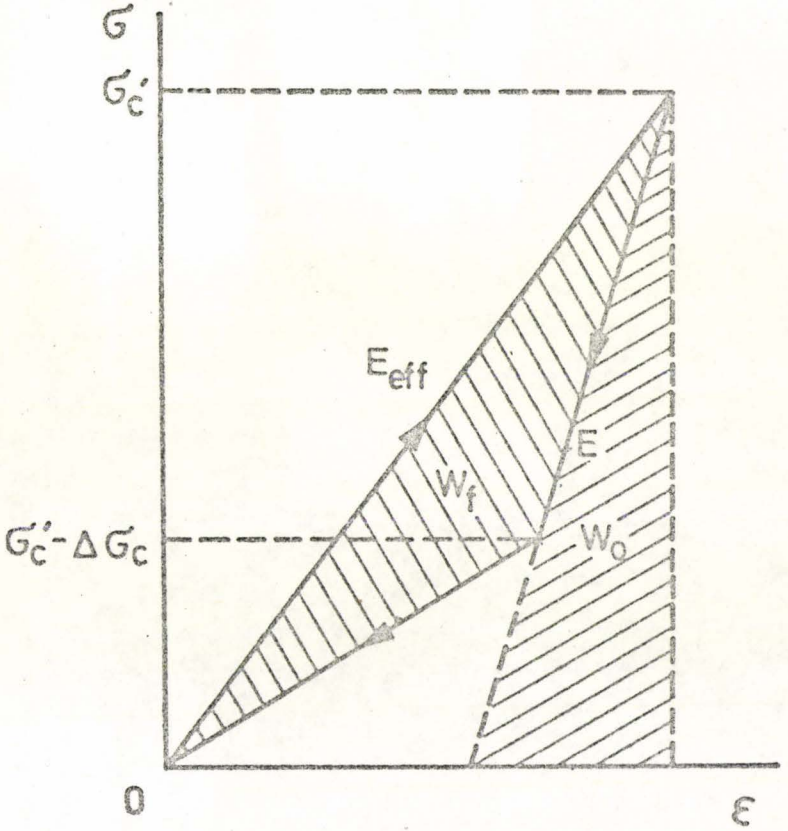

Figure 5 (a)

The Stress-Strain Diagram in Uniaxial Compression for a Body Containing a Single, Inclined, Closed Crack.

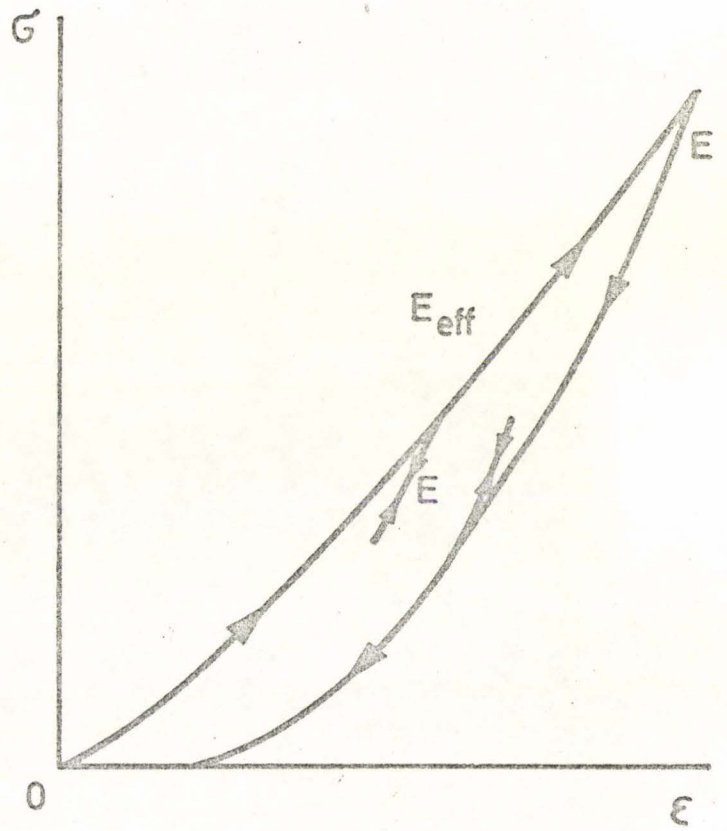

Figure 5 (b)

The First Two Regions of a Complete Stress-Strain Curve for Rock During Loading and Unloading in Uniaxial Compression. After Jaeger and Cook [49].

of stability of this crack as:

$$\varepsilon_g = \sigma_g/E_o + 8L\gamma_o{}^2E_o/\pi\sigma_g{}^3 \qquad (1.22)$$

where σ_g and ε_g are the stress and strain conditions at instability. This concept was first formulated by Berry [51] and the locus is shown in Figure 6. For large values of stress it approaches the Hooke's law line, $\sigma = E\varepsilon$. Furthermore, it has a vertical tangent, defined by $d\varepsilon_g/d\sigma_g = 0$, at the point V, which occurs at a crack length of $C_c = (6L\pi)^{-1/2}$. For cracks greater than this length under constant strain, propagation becomes stable and tends to follow the stability locus instead of extending in a catastrophic manner. That is, for materials that decrease their modulus on crack extension there is a possibility of stable or quasi-static crack propagation.

A fracture-mechanical approach to effect of microcracks on crack propagation under thermal shock conditions has been put forward by Hasselman [52]. He proposed that there can be an alternative approach to a maximum stress criteria for design against thermal shock. When the availability of strain energy for crack propagation is limited by the severity of the shock, the conversion of strain energy into effective surface energy may be complete before structural integrity is lost. This approach is therefore based on the reduction of elastic energy stored at the instant of fracture, which can be brought about by the production of microcracks by microstructural inhomogeneities. Furthermore, since thermal shock is analogous to the fixed-grip condition of crack propagation, "long" cracks can give rise to quasi-static crack propagation after the work of Berry [51]. This effect could limit the amount of crack propagation

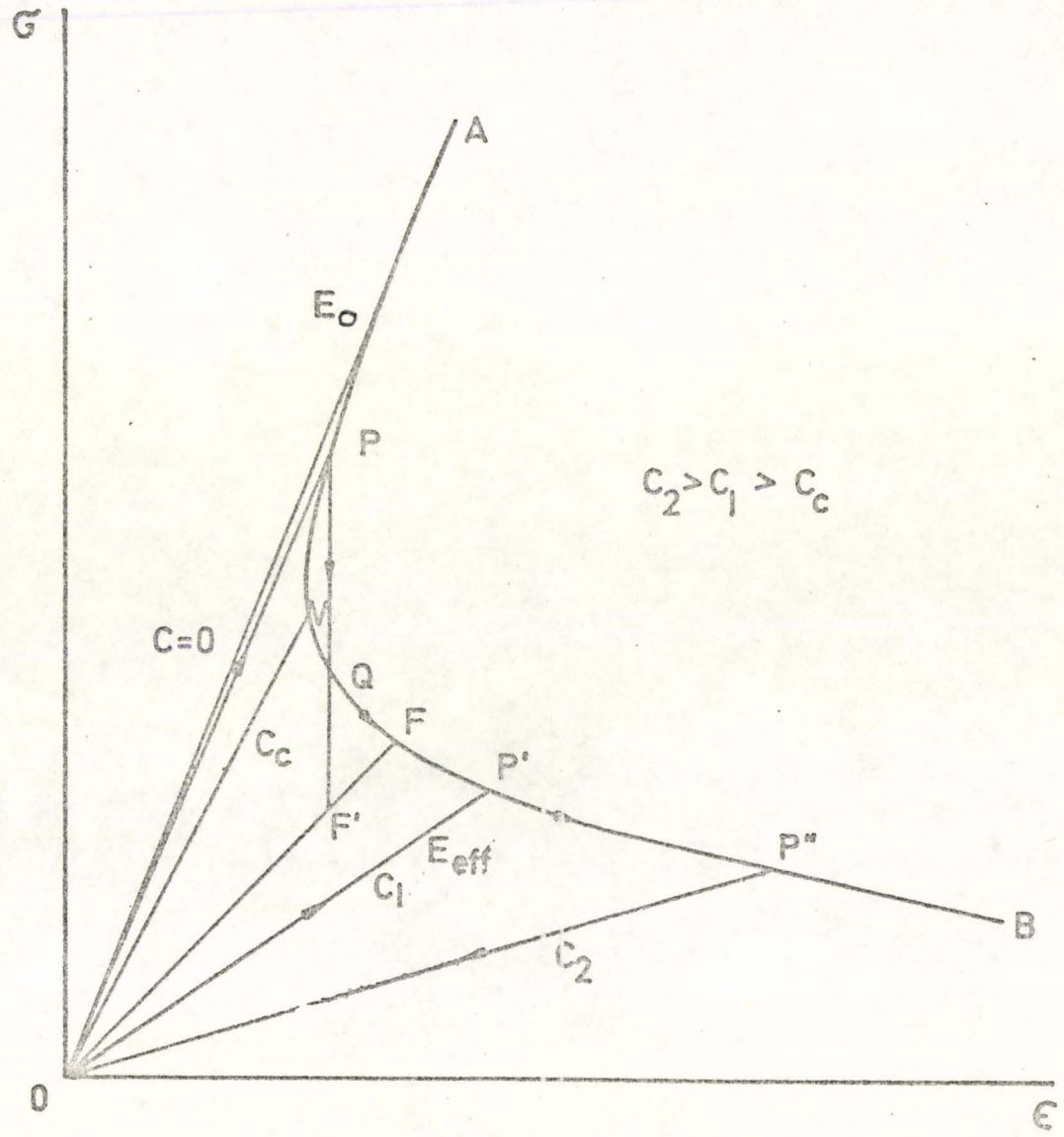

Figure 6. The Stress-Strain Curve Diagram for a Body Containing a Crack, Showing the Effective Young's Moduli for Different Crack Lengths and the Griffith's Locus. After Jaeger and Cook [49].

and result in a more gradual loss in strength for brittle material subjected to thermal shock. This approach to thermal shock "damage" resistance has also been discussed by Clarke et al. [53], who find that the ratio of effective surface energy to elastic energy correlates well with thermal shock resistance.

Evans [54] has suggested that for stable crack propagation the effective surface energy can be shown as a combination of terms:

$$\gamma_I = \psi\gamma_o + \gamma_p + \gamma_s + \gamma_c + \gamma_b \qquad (1.23)$$

where ψ is the geometric factor representing the roughness of the fracture surface, γ_o the thermodynamic surface energy, γ_p is a plastic work term, γ_c is the energy of subsidiary cracking, γ_c is the energy of cleavage step formation [55] and γ_b is an empirical term which applies to materials with blunt cracks [18]. Evans also demonstrated that the plastic term is of prime importance in the fracture of magnesia. For different brittle materials, however, the importance of these different terms should be carefully assessed. For example, in a material which contains microcracks, which may extend into secondary cracks, the increased fracture surface could be the main contributor to the effective surface energy. The interaction of the crack with second phase particles or voids has been treated by Lange [56], who showed that the effective surface energy should increase as the distance between the obstacles is decreased.

The ideal case for fracture mechanics would be the definition of effective surface energy as a material parameter. The influence of any plastic zone and the dependance of effective surface energy on grain

size [57,58], purity [59,60], temperature [57,59-61], environment [62-64], porosity [60,61,65] and possibly strain-rate [66] render this concept invalid except perhaps in the case of a microstructure which is perfectly reproducible and well-defined experimental conditions are available.

The effect of crack length on the effective surface energy is important since it is generally determined for large artificial flaws and applied to evaluate the stress to extend inherent flaws. A change in fracture mode from transgranular to intergranular or a change in the size of the plastic zone could affect this extrapolation. Direct observation of inherent flaws is also important since their recognition may help in their elimination and the consequent improvement of the material. Furthermore, comparison of the observed inherent flaw size and the flaw size calculated when the unnotched fracture stress is substituted into the Griffith equation, can aid the decision whether fracture occurs following the extension of inherent flaws or by some plastic deformation process. In polycrystalline ceramics the inherent flaw size can usually be related to the porosity, grain size, or intergranular cracks. The processes of crack nucleation discussed in Section 1.2.1 could then also be related to the mechanism of formation of the critical cracks.

In most situations, the effective surface energy relates only to the initial motion of the crack. Therefore, if there is any difficulty in creating the critical crack, the effective surface energy will reflect this problem. The energy balance is only defined for cracks with very small radii of curvature. For instance, in metals, it has been shown that cracks of finite radius can alter the stress field in the vicinity of the crack tip [67]. In metals the use of fatigue-cracked specimens

helps to solve this problem. In ceramics, notches tend to have an array of microcracks at their tip and it is important to prove that these microcracks do not hinder crack initiation; that is, they must act as one "sharp" crack, otherwise the experimental technique of notching the samples must be changed [18]. It has been proposed that high values of effective surface energy in glass could be due to multiple crack initiation and tongue formation at the initial crack tip [59]. Subsequent motion of the crack is undefined for rapid crack propagation but for stable crack propagation and crack arrest the fracture toughness parameters can still be measured.

1.2.4 Experimental Techniques for Measuring the Effective Surface Energy

As implied in the previous section, continuum fracture mechanics allows two experimental approches for the determination of effective surface energy. A third method, which has found extensive use in ceramic science, is known as the "work to fracture" technique.

The stress intensity approach makes use of the various mathematical elastic stress solutions for the different testing geometries. The stress intensity calibration for four-point bend specimens (Figure 7), is expressed as a function of applied load, crack size and sample dimensions. The bend test finds extensive use in ceramic testing, since it obviates the need for uniaxial tensile tests with the attendant gripping and alignment problems. At failure, therefore, the critical stress intensity can be calculated from the specimen dimensions, crack size and critical load at failure. The boundary collocation K calibration for pure

ANALYTICAL SPECIMEN FOR FOUR-POINT BEND STRESS INTENSITY CALIBRATION

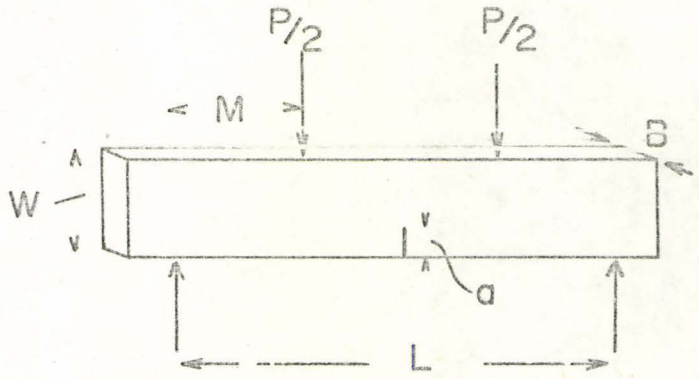

Figure 7. Stress Intensity Calibration for Four-Point Bend Test: Specimen.

bending [68] can be applied to four-point bending if the ratio of the minor span to specimen depth is not less than two and is represented by a fourth-degree polynomial accurate to within 0.2 percent for all values of a/W up to 0.6 [4]. The geometric calibration is:

$$Y = K_I BW^2/6Ma^{1/2} = 1.99 - 2.47\ (a/W) + 12.97\ (a/W)^2 - 23.17\ (a/W)^3 + 24.80\ (a/W)^4 \quad (1.24)$$

and is graphically shown in Figure 8. The ratio of the major support span S to specimen depth W should be greater than 4, otherwise it is difficult to avoid substantial errors from specimen indentation and friction at the supports. Even with ratios of S/W larger than four, it is necessary to take precautions to minimize such errors [4].

The second method, known as the compliance method, is based on equation (1.17). A series of specimens are prepared with a range of crack size and as the specimens are loaded the relative displacements of the loading points are measured as a function of the load for each crack length. Since it is the derivative of compliance that is determined in the calculation of the effective surface energy, the displacements and loads should be measured to a high degree of accuracy [4]. The main limitation of the method is generally the displacement measurements and sensitive strain gauges must be used. The error-magnification effect of differentiation should be less the larger the number of compliance measurements involved for a given range of accurately determined crack lengths. The method is sometimes modified to use the reciprocal of

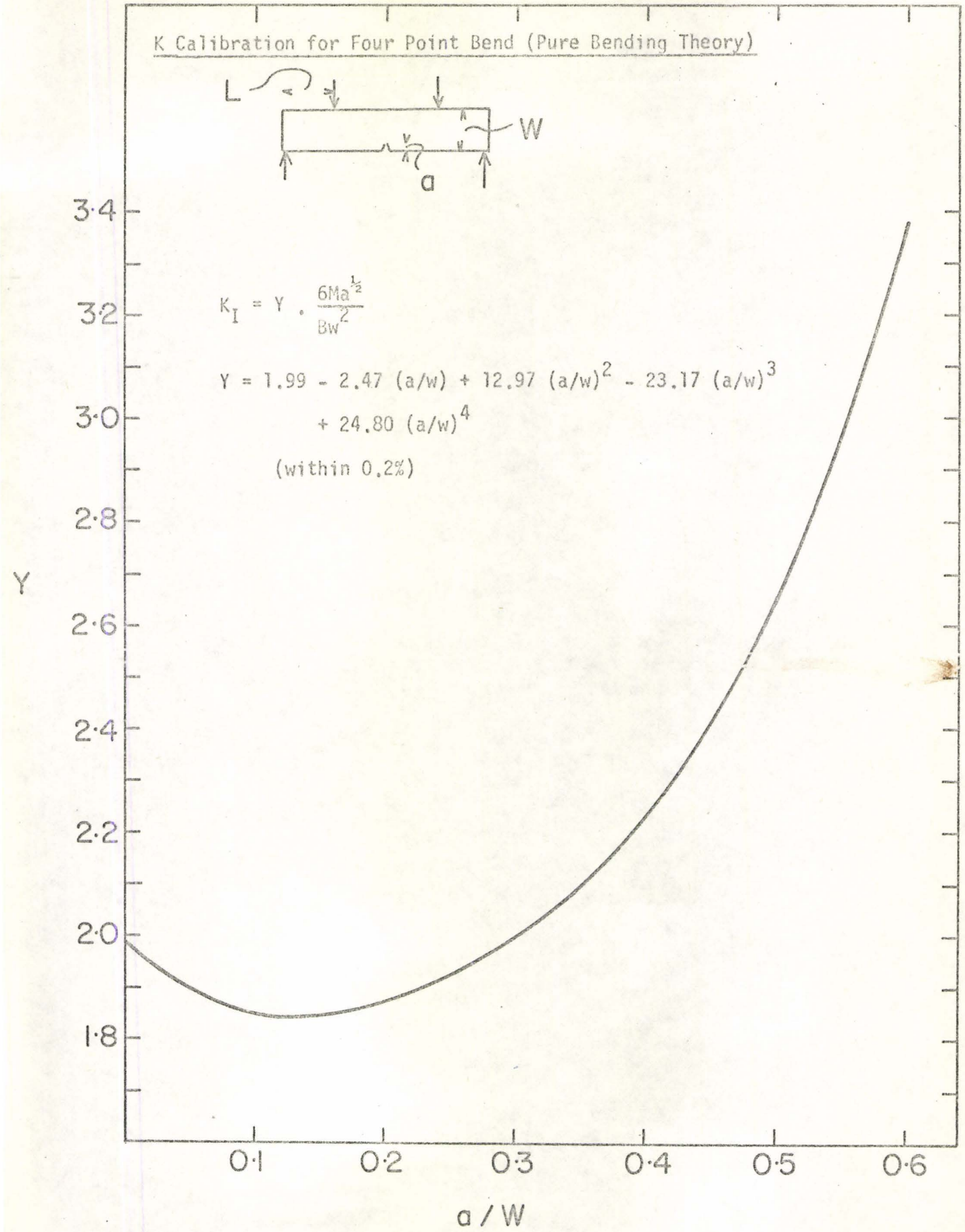
K Calibration for Four Point Bend (Pure Bending Theory)
L
W
a
$K_I = Y \cdot \frac{6Ma^{\frac{1}{2}}}{Bw^2}$
$Y = 1.99 - 2.47\,(a/w) + 12.97\,(a/w)^2 - 23.17\,(a/w)^3 + 24.80\,(a/w)^4$
(within 0.2%)
Y
3·4
3·2
3·0
2·8
2·6
2·4
2·2
2·0
1·8
0·1
0·2
0·3
0·4
0·5
0·6
a / W

Figure 8.

of compliance, i.e., the stiffness [59]. Using a similar approach to the compliance analysis:

$$P = k\delta \tag{I.25}$$

where δ is the deflection of the sample and P is the load. The effective surface energy:

$$\gamma_I = - (\partial U/\partial A) = - (\partial U/\partial k)_\delta \, (\partial k/\partial A)_\delta \tag{I.26}$$

At the point of fracture we know:

$$U = k\delta_F^2/2 \tag{I.27}$$

and therefore:

$$(\partial U/\partial k) = \delta_F^2/2 \tag{I.28}$$

Thus:

$$\gamma_I = - \delta_F^2/2 \, (\partial k/\partial A) \tag{I.29}$$

where δ_F is the deflection of fracture and $(\partial k/\partial A)$ is obtained from the experimental curve of k against A.

Early attempts to measure fracture toughness involved the use of Charpy and Izod impact machines. The energy absorbed per unit area during such a test can be calculated and taken as a measure of the material's toughness. Such tests are somewhat qualitative due to kinetic energy losses, energy integration across the fracture surface and the influence of testing geometry. A more accurate technique, known as the "work to fracture" has been introduced [69] and critically assessed [5] and now

finds application in ceramic testing.

The Griffith energy balance for crack growth can be written:

$$-\partial U/\partial a = \gamma_I \qquad (1.30)$$

When this criterion is fulfilled, it is energetically possible for the crack to grow. Its subsequent behaviour, however, will depend on the value of $(-\partial^2 U/\partial a^2)$. If $(\partial^2 U/\partial a^2)$ is positive the crack will accelerate because the energy released is more than enough to create the new surface involved. If, however, this derivative is negative and if $(-\partial U/\partial a)$ becomes less than the effective surface energy, external work must be done to keep the crack moving. In this latter case, growth of the crack may be controlled and the amount of energy required for propagation can be measured. This situation can be realised in practice for brittle materials of low strength or by limiting the amount of elastic stored energy in strong, brittle specimens and the testing machine at the moment of fracture initiation. This reduction in stored energy is generally achieved using a hard testing machine and a specially shaped notch in the specimen, such as shown in Figure 9. This artificial type of notch, which leaves a triangular area of material, allows fracture to start at low stresses while as the crack propagates, the increasing surface area encountered encourages crack stability. It is argued that all the work done during fracture is represented by the area under the load-deflection curve and is used in the growth of the crack and any related damage. The total work done is simply divided by the cross-sectional area of the fractured specimen to give the work to fracture values (γ_F); no account is taken of fine scale surface irregularities in the area

ARTIFICIAL NOTCH FOR WORK TO FRACTURE MEASUREMENTS

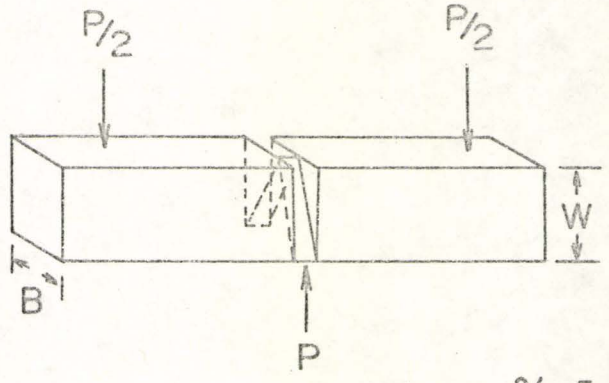

$$\gamma_F = \frac{\text{WORK DONE}}{BW}$$

Figure 9. Sample for Work to Fracture Tests. After Nakayama [69].

estimation. Considerations of the work to fracture are of significance only in loading conditions that give limited strain where a limited amount of energy is available for crack growth. Such is the case for mechanical and thermal shock loading conditions. Paradoxically, a low fracture stress may lead to less damage and therefore reduce the possibility of complete failure. The effect of crack velocity, type of loading and specimen size is shown to affect work to fracture values [5] which is to be expected in limited strain situations.

Finally, it is useful to discuss the philosophical difference between work to fracture values and the effective surface energy. Provided there is no resistance to the formation of the "sharp" crack and no energy loss before the critical load, the effective surface energy will reflect the resistance to initial motion of a stationary crack. In fracture toughness testing of metals and ceramics the critical point is generally taken as the point of rapid crack propagation. If, however, the crack propagation proceeds in a slow, controlled manner, such as in the work to fracture technique, both the work to fracture and effective surface energy can be related to the subsequent motion of the crack and the microstructural aspects of the fracture surface. The work to fracture is determined by an averaging procedure over the entire fracture cross section. In completely brittle ceramics no difference between the work to fracture value and the effective surface energy would be expected since initiation and propagation are indistinguishable. It has been proposed [59] that any difference between these two parameters must be related to physical processes occurring in crack propagation. It is suggested that the effective surface energy

reflects initial crack motion and the work to fracture value, its subsequent motion. For instance, the large values of γ_F compared to γ_I for graphite were explained [59] by the presence of many microcrack sources and the consequent difficulty of crack propagation. Typical values for γ_I and γ_F for ceramic materials are shown in Tables 1 and 2.

The occurrence of stable crack propagation is an interesting phenomena in brittle materials and is generally influenced by three factors [70]: (1) stability due to increasing rate of energy demand such as the formation of a microcrack or plastic zone, (2) stability due to energy release being independent of crack length, or (3) stability when the energy release decreases with increasing crack length. These last two factors are generally a function of the testing geometry and the extension of a "long" Griffith crack in the case of constant strain loading can lead to crack stability.

1.3 Calcia Partially-Stabilised Zirconia

1.3.1 Zirconia

Pure zirconia is a highly refractory oxide with a melting point of 2690°C. The combined properties of chemical inertness, refractoriness and unusual electrical properties, both of zirconia and some of its binary oxide systems, make it a material of major interest. As pointed out by Garvie recently [71], research in zirconia has been characterized by controversy and much clarification is needed

TABLE I

Fracture Energies of Polycrystalline Ceramics

Material	Ref.	Grain Size (μm)	Fracture Energy (10^4 ergs/cm^2)	No. of Tests
99.99% BeO	[116]	3	3.23 ± 0.19	16
99.8 % high strength Al_2O_3	[117]	10	1.82 ± 0.10	11
99.8 % regular Al_2O_3	[117]	30	2.84 ± 0.23	10
99.8 % overfired Al_2O_3	[117]	45	4.76 ± 0.40	10
99.8 % high strength Al_2O_3	[118]	10	1.48 ± 0.39	30
99.8 % regular Al_2O_3	[118]	30	3.57 ± 1.01	31
99.9 % Al_2O_3	[119]	3	2.43	4
85 % Al_2O_3	[119]	15	2.07 ± 0.69	8
$MgAl_2O_4$	[119]	0.3	1.04	2
$MgAl_2O_4$ + 0.01% $CaZrO_4$	[119]	0.3	1.12	4
$MgAl_2O_4$	[119]	6	1.69	5
$MgAl_2O_4$ + 0.01% $CaZrO_4$	[119]	6	0.91	3
SiC	[119]	40	3.24 ± 0.64	9
Graphite .	[119]	<25	6.81 ± 0.45	22
Si_3N_4	[120]		2.6	
UO_2	[58]	8	0.8	
MgO	[60]	25	1.4	

TABLE 2

Work to Fracture Values for Various Materials

Material	Ref.	Work to Fracture (erg/cm^2)
Dural	[5]	1.4×10^8
Copper	[5]	5×10^7
Key Steel	[5]	5×10^7
Brass	[5]	3×10^7
Teak Wood	[5]	6×10^6
Toughened Polystyrene	[5]	4×10^6
Deal Wood	[5]	2×10^6
Cellulose	[5]	2×10^6
Polystyrene	[5]	10^6
Reactor Graphite	[5]	10^5
Firebrick	[5]	$2\text{-}7 \times 10^4$
Alumina	[59]	3.0×10^4
Mica Glass Ceramics	[22]	3.0×10^4
Beryllia	[5]	2×10^4
Magnesia	[5]	10^4
Glass	[59]	7×10^3

before the properties are understood and can be applied practically.

Zirconia exists in three polymorphs, namely, monoclinic, tetragonal and cubic. The monoclinic phase is stable up to about 1000°C and then transforms over approximately a 100°C temperature range to the tetragonal phase. Finally, at approximately 2370°C, the tetragonal phase adopts the cubic fluorite structure. It is quite surprising that zirconia crystallises in the fluorite structure or derivatives of this structure from considerations of the radius ratio of the ions. The radius ratio of zirconia is 0.57 and should be well within the rutile field [72]. It has been suggested [73] that there must be appreciable covalent bonding in zirconia to account for this paradox.

The lattice parameters for monoclinic zirconia have been determined by Adams and Rogers [74] and are as follows:

$a = 5.1454 \pm 0.005$ Å

$b = 5.2075 \pm 0.0005$ Å

$c = 5.3107 \pm 0.0005$ Å

$\beta = 99.14' \pm 0.05'$

Space group = $P2_1/C$

The zirconium ions are in seven-fold co-ordination and are sandwiched on one side by oxygen ions in tetragonal co-ordination and on the other by oxygens in triangular co-ordination [75]. An idealised arrangement is shown in Figure 10. The structure was refined by Smith and Newkirk [76] but is practically the same as the idealised structure except for a slight distortion in bond angles and lengths.

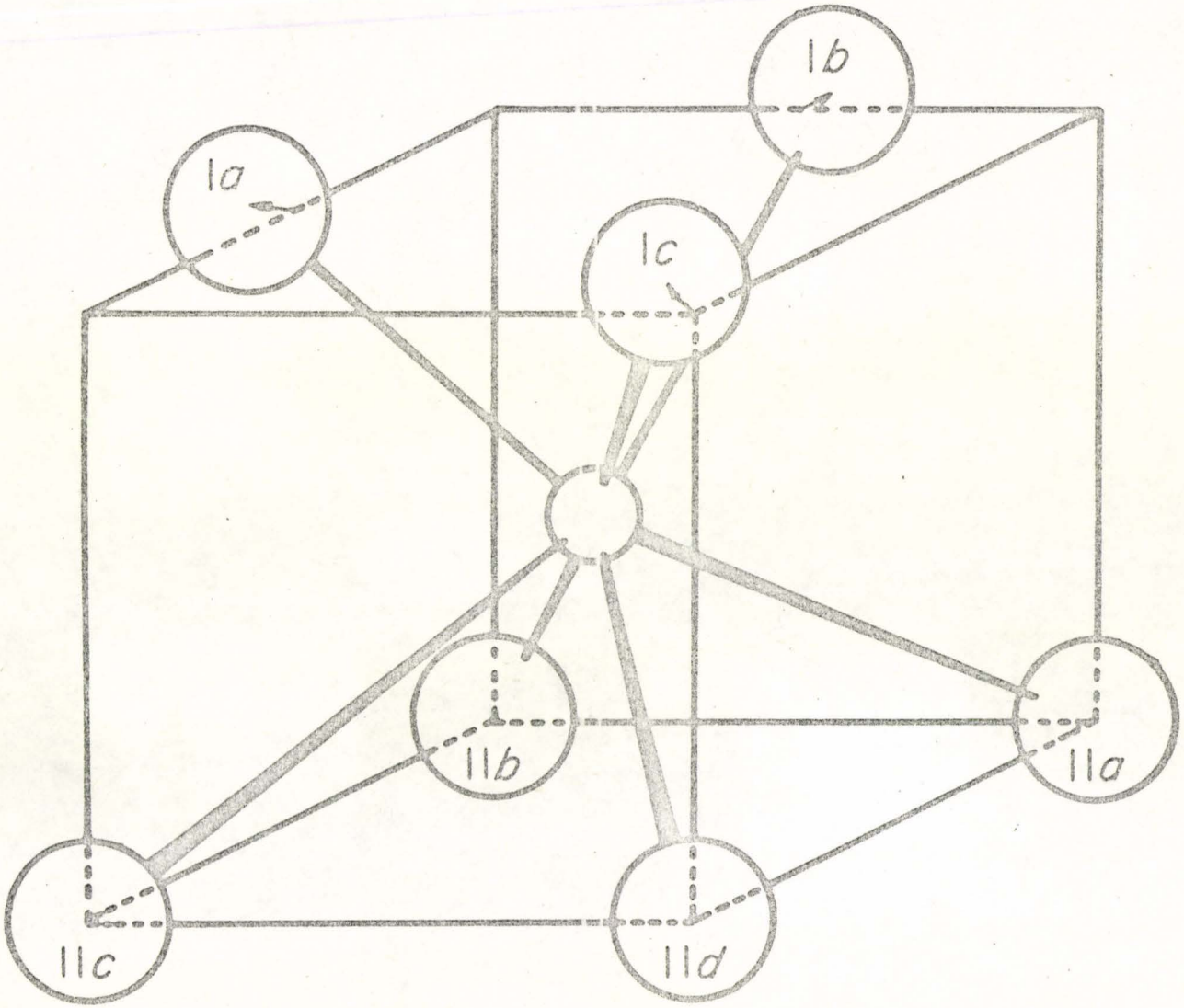

Figure 10. Idealised Crystal Structure, Monoclinic Zirconia. After McCullough and Trueblood [75].

Tetragonal zirconia is stable at normal pressures above 1100°C and cannot be retained on quenching. A metastable form, however, has been observed at room temperature when zirconia is produced by certain techniques. For instance, if zirconia is prepared by calcining a chloride at low temperatures, the tetragonal form can be produced. Garvie [71] explained this phenomena on the basis of a crystallite size effect since the surface energy associated with finely-divided powders could lead to this metastability. There has been recent confirmation [77] that this mechanism is reasonable.

The crystal structure of tetragonal zirconia was determined by Teufer [78], who obtained the following results at 1250°C:

$$a = b = 3.64 \text{ Å}$$

$$c = 5.27 \text{ Å}$$

Space group = $P4_2/nmc$

The properties of the tetragonal and monoclinic phases have been well reviewed by Garvie [71].

The first evidence of the existence of cubic zirconia was reported by Smith and Cline [79]. The inversion was placed at 2285°C but this has been corrected to 2370°C in a private communication to Viechnicki and Stubican by Smith [80]. The cubic phase cannot be retained on quenching. The very existence of this phase in pure stoichiometric zirconia has been disputed by Weber [81] since the zirconia could lose oxygen or be contaminated by metal impurities at these temperatures. The work of Ruh and Garrett [82], however, on the phase diagram of zirconium and oxygen, is consistent with the existence of the cubic form of pure

stoichiometric zirconia. The lattice parameter of cubic zirconia at 2300°C has been shown to be 5.273 Å [79].

1.3.2 The Monoclinic-Tetragonal Phase Transformation

The first significant research on this phase transformation was contributed by Wolten [83], in which he clearly described its non-quenchable, diffusionless reversible, athermal nature. The transformation occurs with considerable temperature hysteresis and is shown in Figure 11. These characteristics are similar to the martensitic phase transformations observed in metals in which the growth of the product crystal takes place by the systematic co-ordinated movement of atoms in the parent crystal in such a way as to generate the product structure. The atoms in such a transformation move a fraction of one lattice spacing and any atom tends to have the same neighbours in the product as in the parent phase. Wolten described the transformation as "brittle-martensitic" since zirconia is too brittle to sustain any plastic deformation and tends to crack instead. Bailey [84], however, notes that in the monoclinic to tetragonal transformation the accommodation strains are relieved entirely by slip, whereas the reverse transition from tetragonal to monoclinic involves intergranular cracking. Furthermore, Bailey notes that in this reverse transformation constrained monoclinic grains tend to twin on the (100) or {110} planes. This final observation has been confirmed by Heuer [85] and both Bailey and Heuer observe that approximately 50% of the monoclinic is twinned.

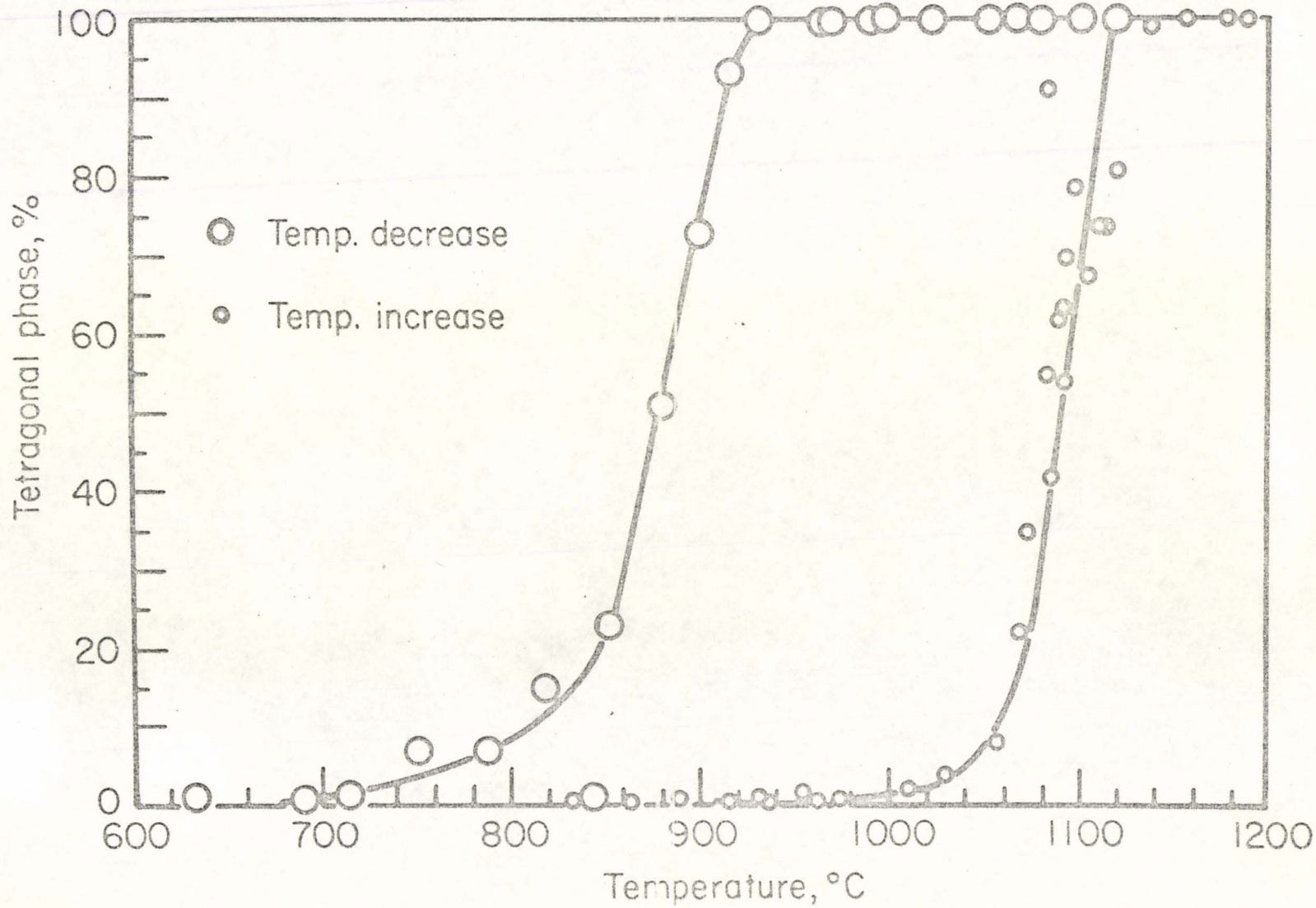

Figure 11. Monoclinic-Tetragonal Transformation in Zirconia. After Wolten [83].

The transformation involves a large shape and volume change (9% increase in volume tetragonal to monoclinic) as expected due to its martensitic nature. The shape deformation in a martensitic transformation may be regarded as a simple shear parallel to the plane of the martensite platelet plus a contraction or expansion normal to the plane of the platelet. The shape deformation involves considerable elastic distortion which constrains growing crystals to form a platelet-acicular microstructure. Such a microstructure has been observed in zirconia heated to 1300°C and then cooled under observation by Fehrenbacher and Jacobson [86]. From their metallographic observations of the transformation they concluded that the transformation is of the Fe-Ni type which also has a large associated temperature hysteresis. Bailey [84], however, on his electron microscope work on thin films, noted that the interface could move in many directions but concluded that this may be an artifact of the foil since the volume change is quite large and must involve considerable strain. Bailey also noticed the absence of fine scale twinning, which is generally observed in Fe-Ni type transformations. Heuer [85] followed the transformation by preparing foils from the bulk material using an ion-bombardment technique. He also noticed the absence of fine-scale twinning and found twins of width 0.05 μ to 0.2 μ. Heuer concludes that the transformation tetragonal to monoclinic is more likely to be of the In-Tl type which gives rise to single sets of parallel twins. More recently, however, Bansal and Heuer [87] have shown that the invariant shear occurs by slip in the tetragonal phase and not by twinning in the monoclinic phase. The twinning observed in the monoclinic phase is thus believed to be deformation twinning which arises because of the accommodation stresses generated in

the transformation. In this work Bansal and Heuer determined the habit plane to be (010) (referred to the monoclinic phase) and now believe the transformation to be of the Fe-Ni type.

The observations of the lattice invariant deformations of slip and twinning by Bailey are not surprising since in general the homogeneous strain observed in martensitic reactions when applied to the parent lattice does not generate the product lattice. Additional, minor deformations of slip and twinning combined with the homogeneous lattice deformation, however, can account for the final position of the atoms.

Since the atomic movements in the transformation are co-ordinated there is always an orientation relationship between the two phases. The orientation relationships observed in zirconia are [76,84]:

$$(001)_m \;//\; (001)_t$$
$$(100)_m \;//\; (110)_t$$

though for the work of Bailey [84], it is necessary to correct for his use of the large face-centred cell rather than the conventional cell. The relationship between the monoclinic and tetragonal phase is complicated and requires the severing of some bonds. The large hysteresis observed in the transformation is indicative of the semi-reconstructive nature of the atomic re-adjustments. Smith and Newkirk [76] proposed that the whole transformation takes place by the rotation of the triangular group of oxygen ions in the (100) planes plus some minor atomic movements into the more symmetrical positions as shown in Figure 12.

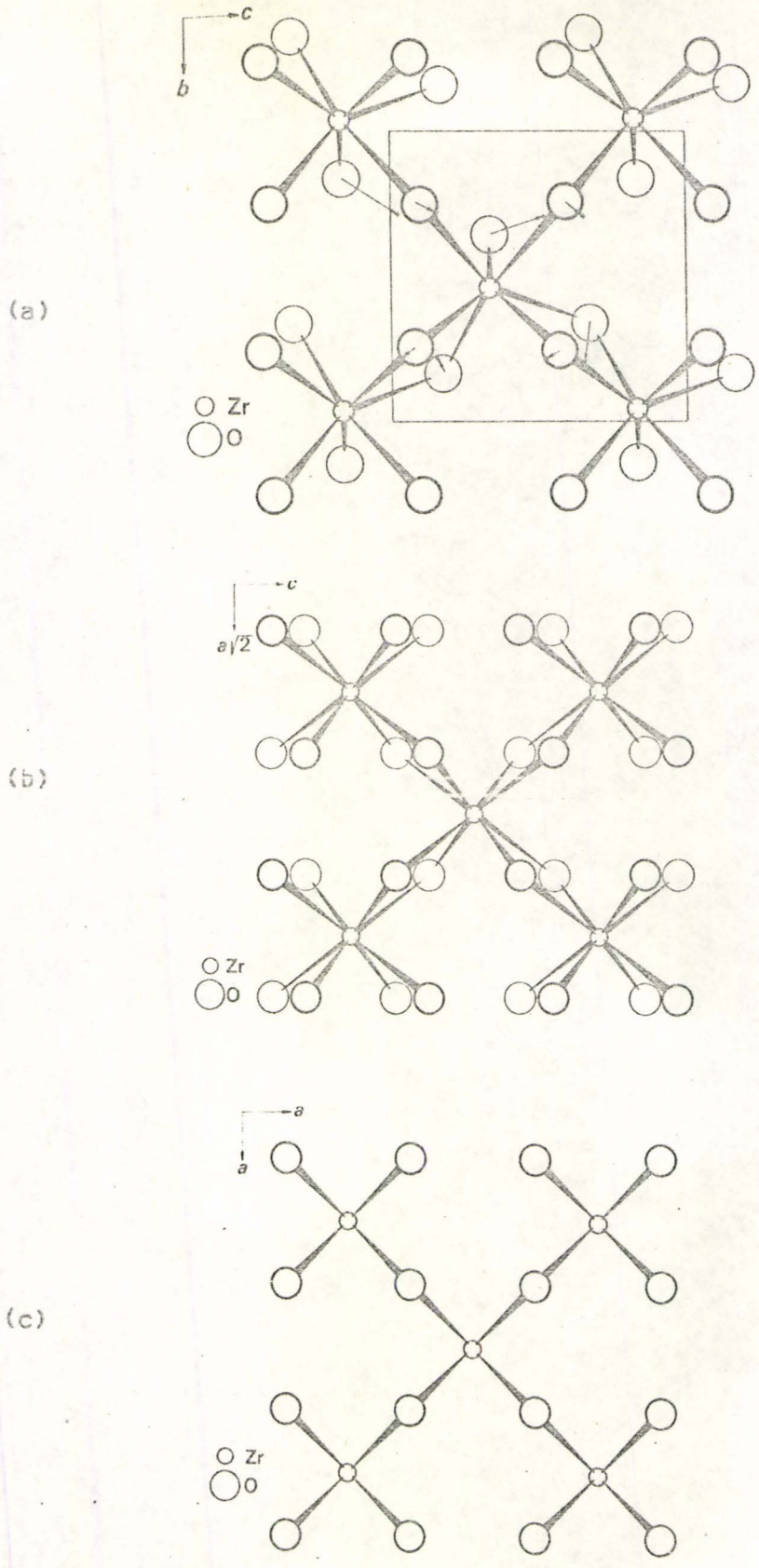

Figure 12. The Crystal Structures of Pure Zirconia, (a) monoclinic, (b) tetragonal, (c) cubic. The arrows in the monoclinic structure indicate atom movements in the martensitic monoclinic to tetragonal transformation. After Smith and Newkirk [76].

Grain and Garvie [88] have proposed a mechanism for the transformation based on Ubbelohde's theory of continuous transformation [89]. This involves the formation of tetragonal domains in the monoclinic crystals. These domains are oriented to satisfy crystallographic relationships, with the associated strain energy giving rise to the hysteresis and the athermal nature of the transformation. Heuer [85] disputes this and has shown the transformation to be an orthodox martensitic transition.

Since martensite transformations involve a change of shape in a finite volume of matter, applied stresses can influence the reaction. The acting stress system should be resolved into components parallel to the shear and dilational displacements of the transformation, both of which will affect the transformation temperature. The mechanical work done on or by the transforming region, as the resolved components of the acting stress are carried through the corresponding transformation strains, is added algebraically to the chemical free energy of the reaction in order to compute the alteration in temperature at which the critical value of the driving force to start the transformation is attained [90]. The transformation temperature is either raised or lowered depending on whether the mechanical work aids or opposes the chemical driving force.

For hydrostatic pressure, there are generally no shear-stress components to influence the reaction and the pressure interacts only with the dilational strain. In monoclinic systems, however, some of the shear components in the hydrostatic stress tensor are non-zero

[91]. Therefore since the monoclinic to tetragonal transformation involves a volume decrease, pressure can aid both the shear and dilational displacements, and the transfomation should be noticeably pressure-sensitive.

Dow Whitney [92] studied this pressure sensitivity. Using thermodynamics he determined that:

$$- \Delta G(1,T) = \int_{1}^{P} \Delta V\ (P,T)\ dP \qquad (1.34)$$

where $\Delta G(1,T)$ is the free energy change at a pressure of one bar and temperature T, ΔV is the molal volume change for the transformation and P is the pressure. When the foregoing expression is solved for pressure at a given temperature, the point on the P-T diagram at which monoclinic and tetragonal zirconia are in equilibrium is found. Thus the pressure-temperature phase diagram can be calculated with a knowledge of the molal volumes of the phases and $\Delta G(1,T)$. An expression for $\Delta G(1,T)$ can be found from the Gibbs-Helmholtz equation:

$$\left(\frac{\partial \Delta G(1,T)/T}{\partial T} \right)_P = \frac{- \Delta H\ (1,T)}{T^2} \qquad (1.35)$$

where ΔH is the molal enthalpy difference for the two phases.

Dow Whitney calculated the slope of the equilibrium line to be -3.02×10^{-2} degrees/bar as shown in Figure 13. He went on to verify his calculations by electrical resistance measurements up to 15 kbars [93]. Further verification was presented by Kulcinski [94], who found the tetragonal phase could be formed directly at room temperature with a

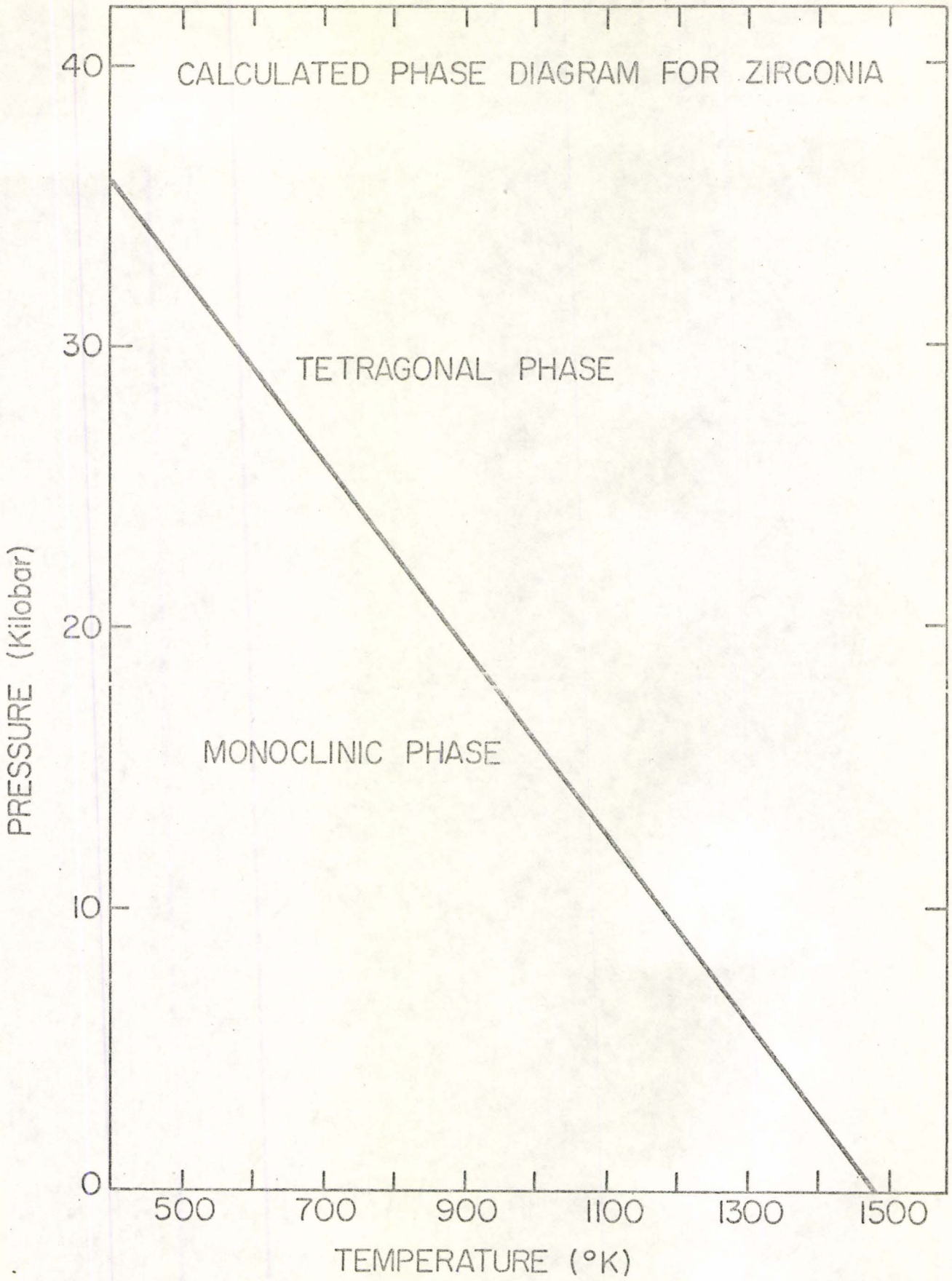

Figure 13. After Dow Whitney [92].

pressure of 37 kbars. .This figure agrees with an extrapolation of Dow Whitney's calculation. Kulcinski also noted that the transformation is completely reversible, cannot be quenched to ambient pressures and impurities have little effect on it at room temperature.

The refractory usage of pure zirconia is limited by this phase transformation, which leads to deleterious residual stress or the formation of intergranular cracks on slow cooling and complete disintegration on shock cooling. It has been found, however, that certain oxides such as calcia, magnesia and yttria can "stabilise" zirconia in a defect fluorite structure, so eliminating the catastrophic transformation.

1.3.3 Calcia Stabilised Zirconia

The phase diagram for the calcia-zirconia system is still much in doubt and regions of it are unexplored. Several attempts have been made to construct this diagram and these can be divided into two groups. In the first group [95-97] no compound was reported in the cubic field and the associated diagrams are shown in Figure 14. The pairs of hatched lines indicate the extent of the cubic field and outside these lines are the two-phase regions. Garvie [98] criticises these three attempts since they tend to use the disappearing phase technique or they are clouded by the metastable existence of the cubic phase.

In the other group of research on the cubic field [99-100] the existence of a compound $CaZr_4O_9$ has been reported at 20 mole percent

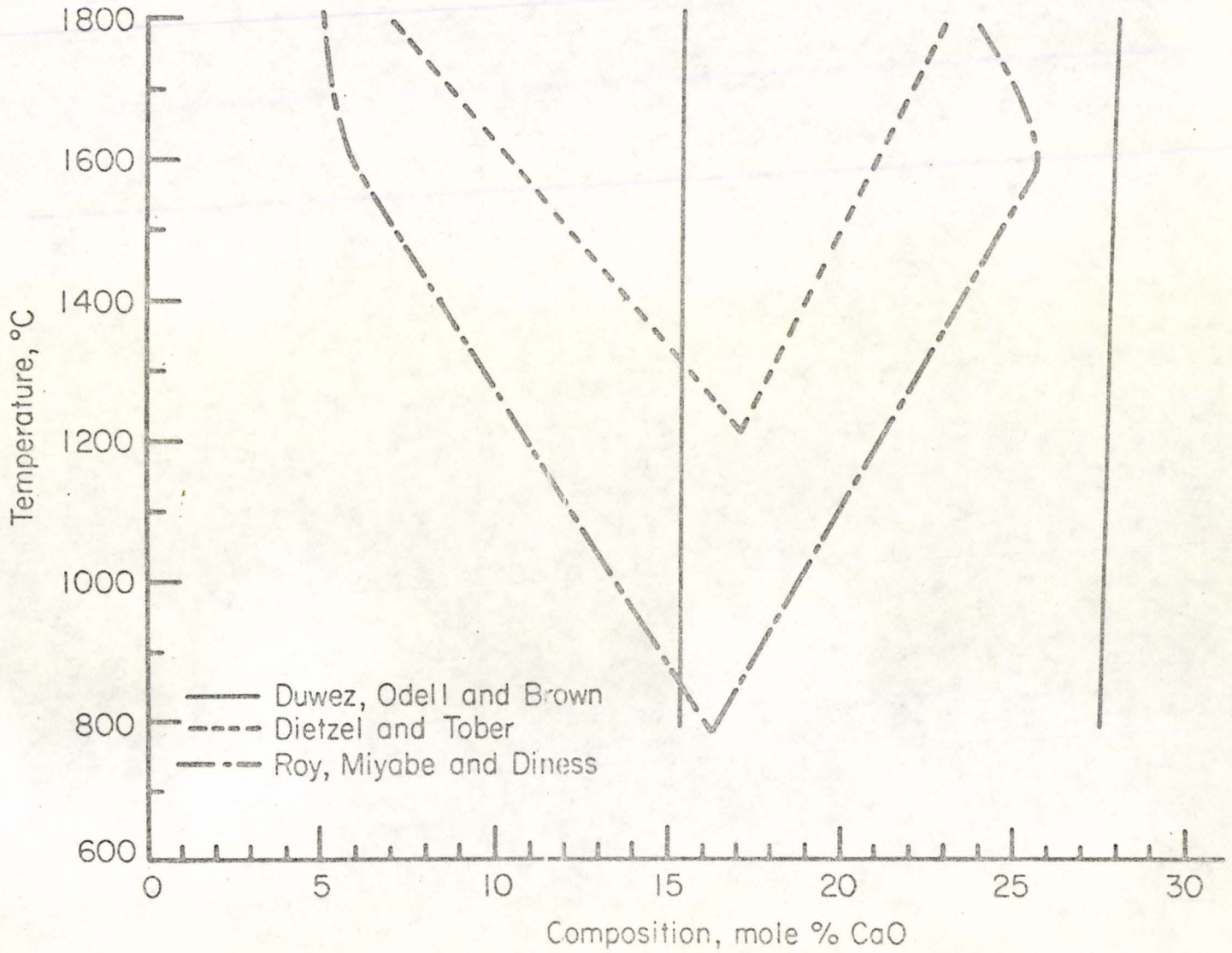

Figure 14. Cubic Fields in System CaO-ZrO_2 which Show no Compound Formation [95-97].

CaO and the cubic field was therefore proposed to consist of solid solution of zirconia in $CaZr_4O_9$ (Figure 15). The existence of such a compound is thought to be consistent with the fact that calcia-stabilised zirconia is far more stable than the magnesia-stabilised material, in which no compound is formed. Both workers used reagents $CaCO_3$ and ZrO_2 with Barbariol [99] using the disappearing phase technique and Garvie [98] again criticised both these attempts. It is difficult to envisage, however, either molecular group existing in the other as host, in view of the large size of each molecule.

Since no group of workers agreed, Garvie [98] attempted a new study using an accurate lattice parameter technique and well-crystallised pure oxide reagents. Garvie found further proof of the existence of a compound at 20 mole percent calcia and also showed that the use of $CaCO_3$ can lead to an enlargement of the cubic field so forming a metastable cubic phase. The existence of the compound is further supported by Pyatenko [101], who deduced that a compound should exist at 20 mole percent by a theoretical crystal chemistry argument and by Delamarre and Perez y Yorba [102] who reported the compound $CaHf_4O_9$ in the analogous calcia-hafnia system. Garvie also noticed the possibility of a phase change in the compound at 1700°C since there was a discontinuity in the lattice parameter. The work of Garvie is summarised in Figure 16 and though the cubic field seems well defined the behaviour at lower temperatures is still open to some speculation especially since the cubic material can exist indefinitely at room temperature.

The decomposition of the cubic phase is very important in stabilised zirconia since this can drastically affect the properties of the material.

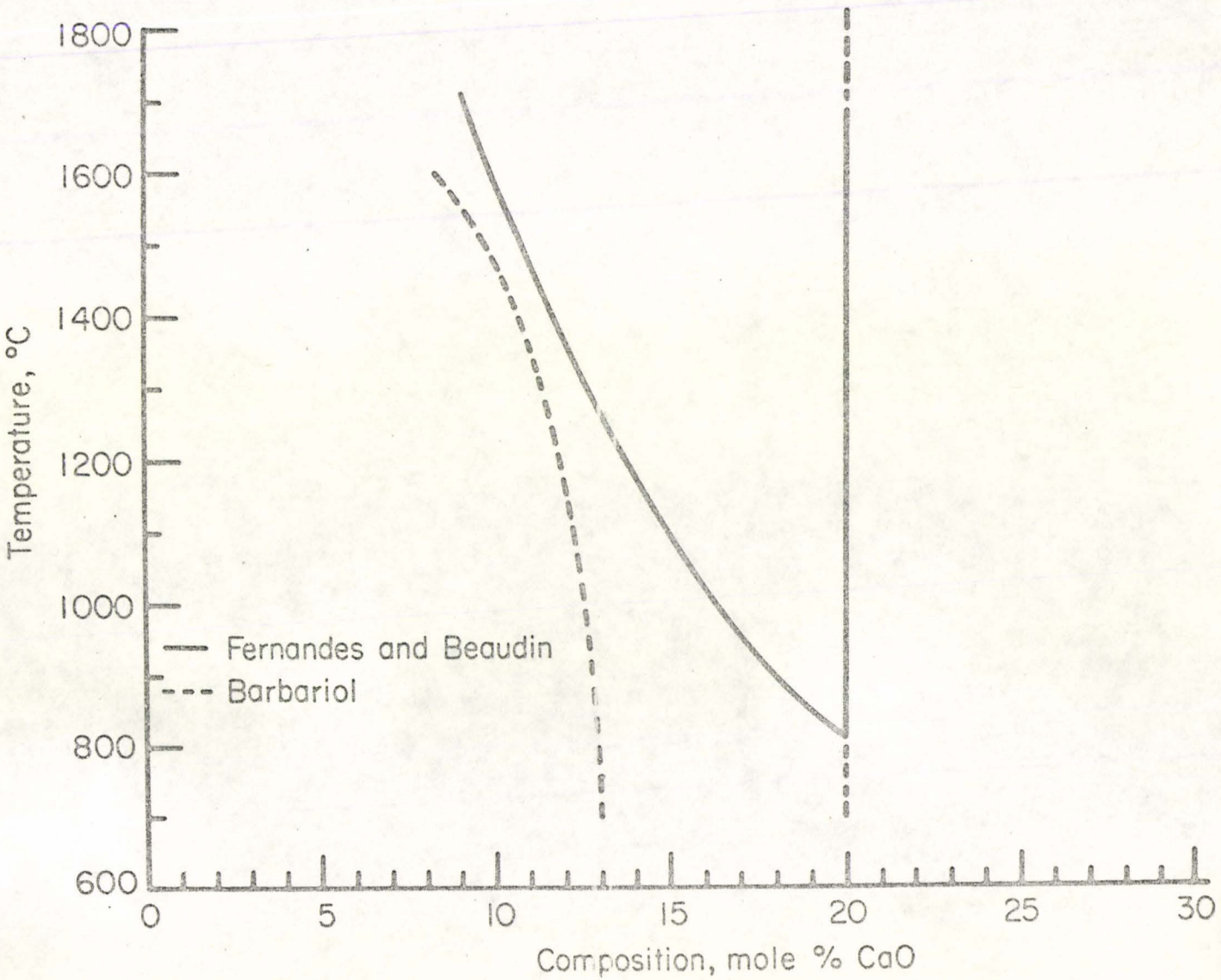

Figure 15. Cubic Fields in System CaO-ZrO_2 which Show Compound Formation [99-100].

FIG. 16 PARTIAL PHASE DIAGRAM FOR THE $CaO-ZrO_2$ SYSTEM.

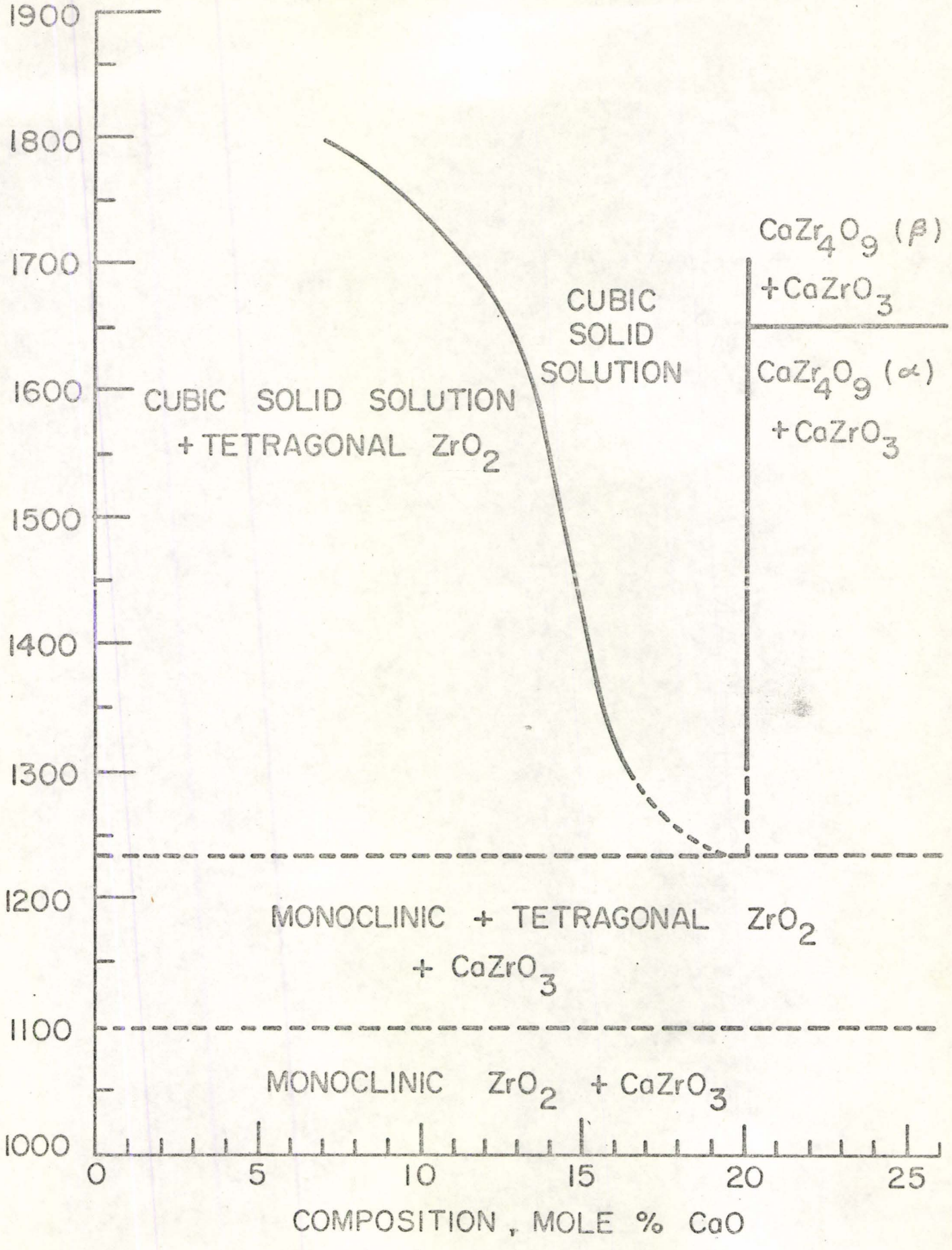

For example, magnesia-stabilised zirconia has been shown to decompose readily on thermal cycling [80]. In calcia-stabilised zirconia destabilisation can be considered as precipitation of zirconia from the solid solution or decomposition of the cubic phase depending on the interpretation of the phase diagram. The precipitation of zirconia will be a function of the degree of supersaturation and this concept is supported by Sukharevski [103], and his co-workers. Their data is summarised in Figure 17. The decomposition of the cubic phase occurs at temperatures below 1200^{o}C and will therefore be a slow process. Roy and his colleagues [97] observed this reaction using water as a catalyst.

From these observations it would appear that only minor decomposition of calcia-stabilised zirconia occurs and this renders this material the preferred system for zirconia ceramics. The physical properties of calcia-stabilised zirconia have been reviewed by Garvie [71] but it should be mentioned that its low thermal conductivity, high thermal expansion values make this material sensitive to thermal shock.

1.3.4 Calcia Partially-Stabilised Zirconia

Vastly improved thermal shock resistance has been noted [104-106] for compositions containing insufficient stabilising oxide to produce 100% cubic phase. These compositions give products known as partially-stabilised zirconias (PSZ) and are two-phase containing the monoclinic or tetragonal

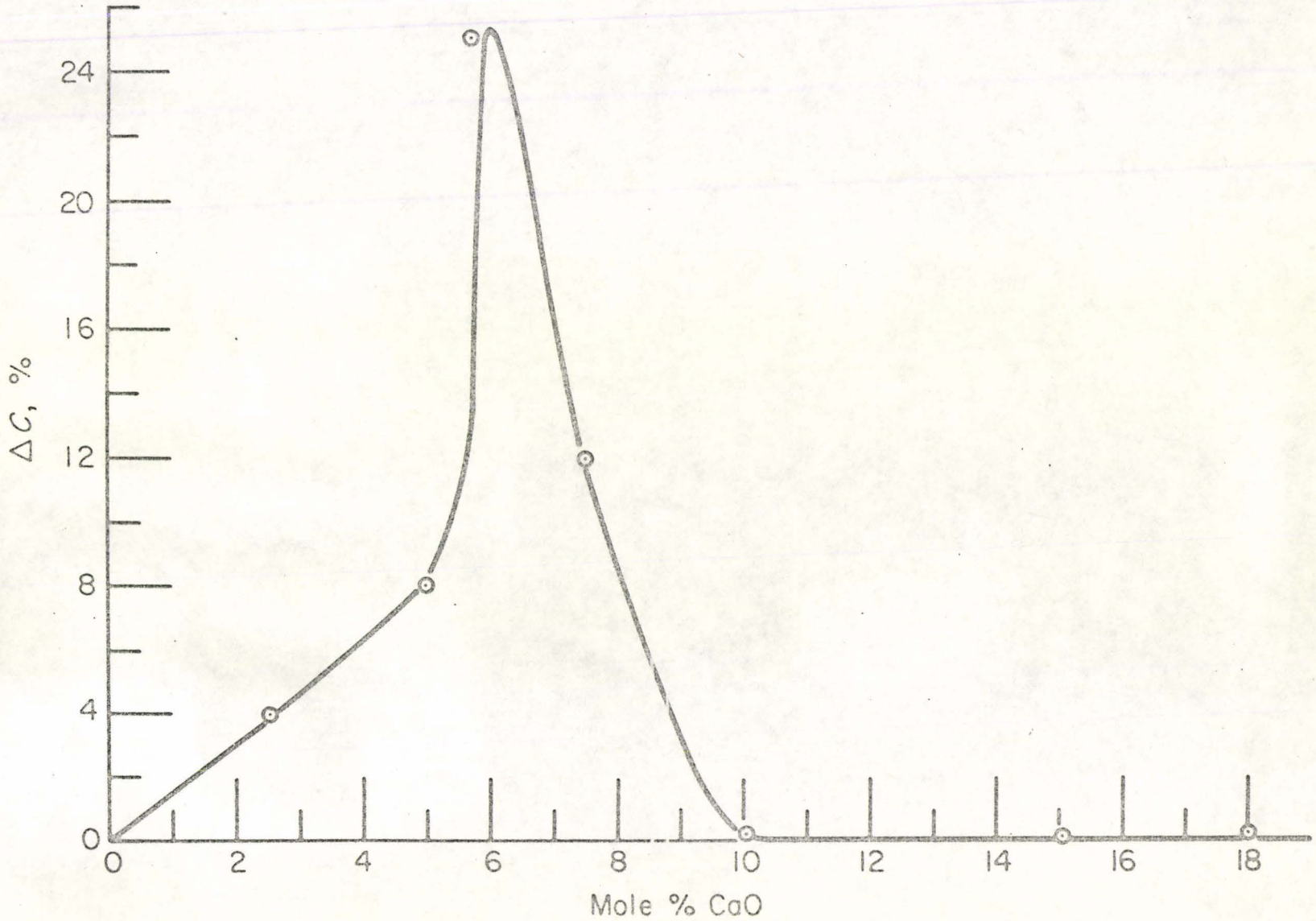

Figure 17. Decrease in Amount of Cubic Phase in Slowly Cooled Samples as a Function of Composition. After Sukhavevski [103].

and cubic phases. The importance of the earlier section on the crystal structures and phase transformation of pure zirconia is now apparent since PSZ contains amounts of free zirconia.

PSZ is generally fabricated by firing carefully mixed ingredients into the single cubic solid-solution field and then allowing precipitation of pure zirconia in the cubic matrix as the system is cooled and becomes supersaturated with zirconia. The mechanism and morphology of the precipitation has not been studied in detail for calcia PSZ. There has, however, been some observations in magnesia PSZ. King and Yavorsky [106] observed petrographically that the monoclinic phase disappeared at 2.8 wt.% MgO, but the material still contained 68% monoclinic at this point based on X-ray measurements. They concluded the monoclinic material must be present as fine precipitates and that this intimate two-phase mixture acted in a grossly mechanical sense as single crystal. This supposition they based on the evident observations of lines in these two phase grains. More recently Jaeger and Nickell [107] observed two types of precipitation in 2.8 wt.% magnesia PSZ. Optically, they observed 20 - 25% of discontinuous small grained monoclinic phase dispersed in the large-grained cubic matrix. The remaining monoclinic phase, they noted, exists as a submicroscopic precipitate or "domain" within the cubic phase with an average diameter of 2000 to 5000 $\mathring{A}$ as shown in Figure 18.

The martensitic transformation should play an important role in the thermo-mechanical properties of PSZ since it produces a very large increase in volume of the precipitate as the ceramic is cooled. King and Yavorsky [106] estimated the stress sustained by the cubic matrix to be 400,000 psi. Furthermore, they observed evidence of stress relief in the

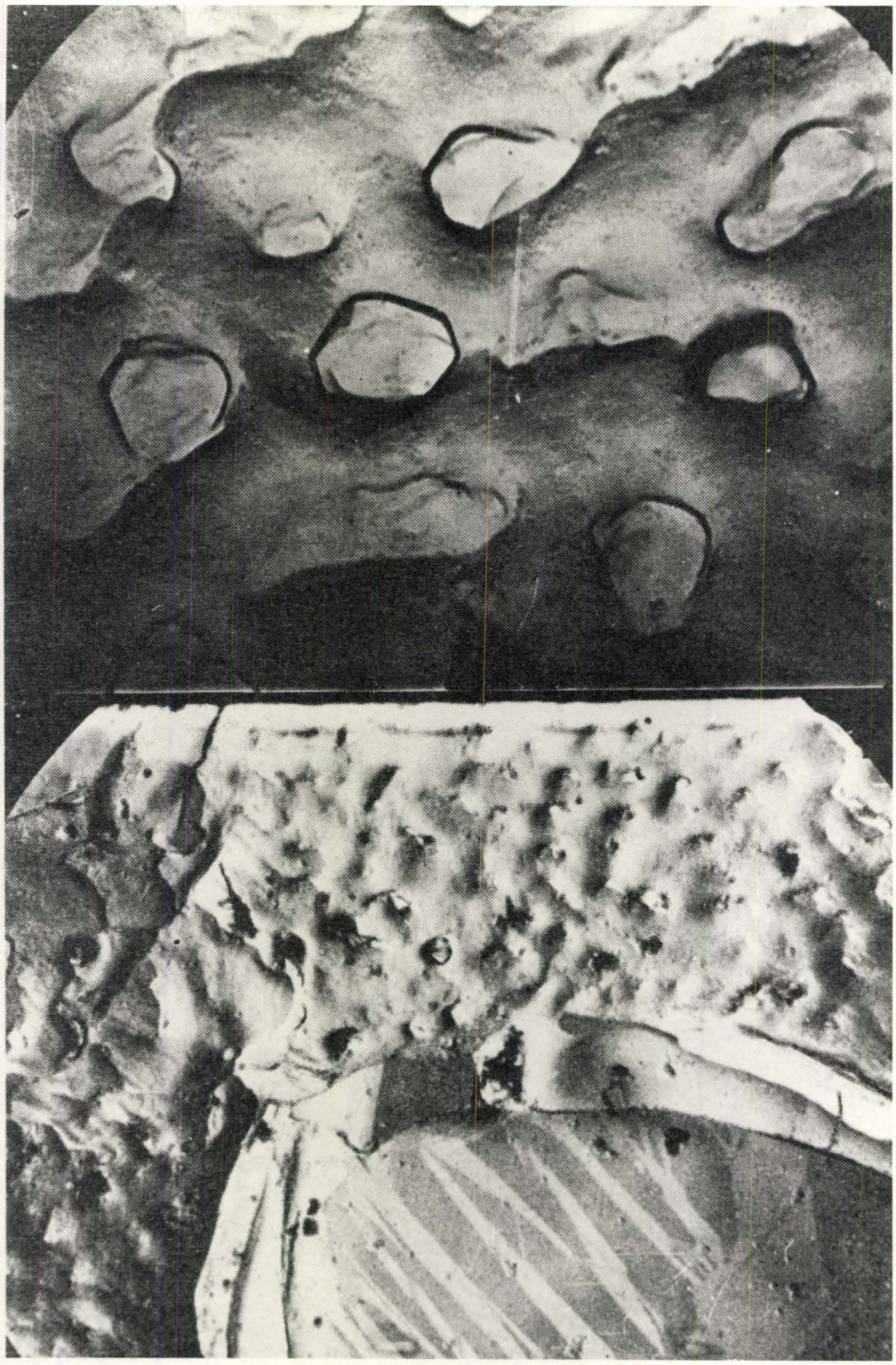

Figure 18. Electron Micrographs of As-Fired Replica Illustrating Multi-phase Microstructure. After Jaeger and Nickell [107].

form of slip around monoclinic inclusions and stress concentrations around pores in both magnesia and calcia PSZ [108]. In the case of magnesia PSZ King and Yavorsky [106] also measured the microhardness (Figure 19). The hardest materials were very brittle and tended to fracture during testing giving the lowest values at the highest magnesia contents. The hardness values measured in the centre of grains increase above ≈ 3% magnesia. They also observed a differential hardness between grain boundaries and centres indicating some solute segregation at the grain boundaries.

The pressure sensitivity of the transformation is also thought to play a role in the thermal shock resistance of calcia PSZ. Garvie and Nicholson [6] also observed the fine precipitation of the monoclinic phase. On thermal cycling, even below the transformation temperature they observed cracks around these submicroscopic precipitates. Garvie and Nicholson proposed that the transformation can be triggered at these temperatures by the thermal stress, resulting in the formation of a high density of microcracks around the precipitate particles. This could then account for the observed thermal shock resistance of calcia PSZ.

There seems to be very little data on the physical and chemical properties of calcia PSZ, though some information can be gleaned on the mechanical properties from papers that discuss the variation of stabilising agent in stabilised zirconia [109-111].

Whittemore and Ault [112] have measured the thermal expansion of PSZ (Figure 20). The complex shape of the curve is due to the combined effects of the cubic and the transforming monoclinic phase. The expansion curve is about midway between pure zirconia and the fully-stabilised material. Similar observations have been made by Jaeger and Nickell [107]

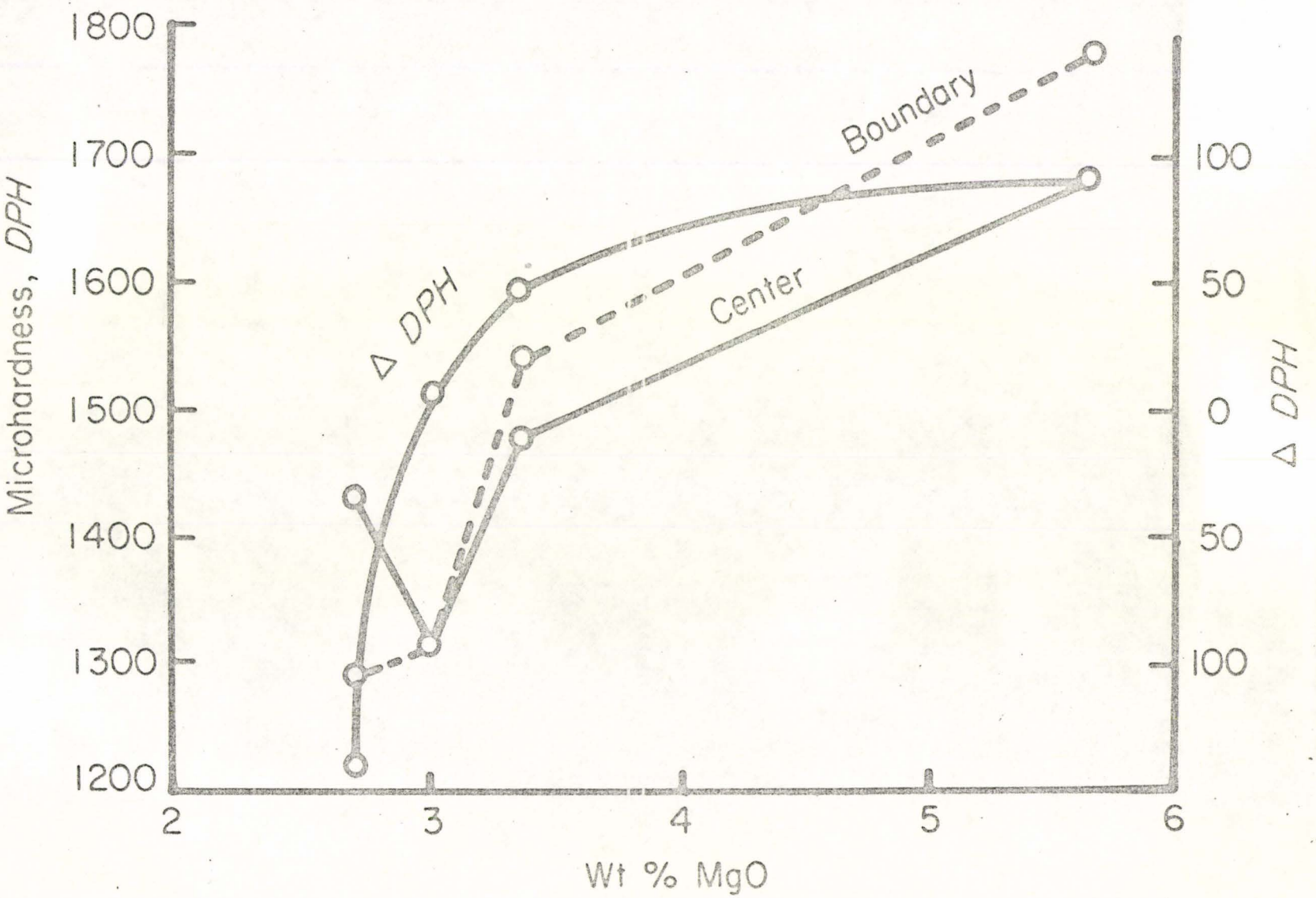

Figure 19. Microhardness Results as a Function of wt.% Magnesia Additions to Zirconia. After King and Yavorsky [106].

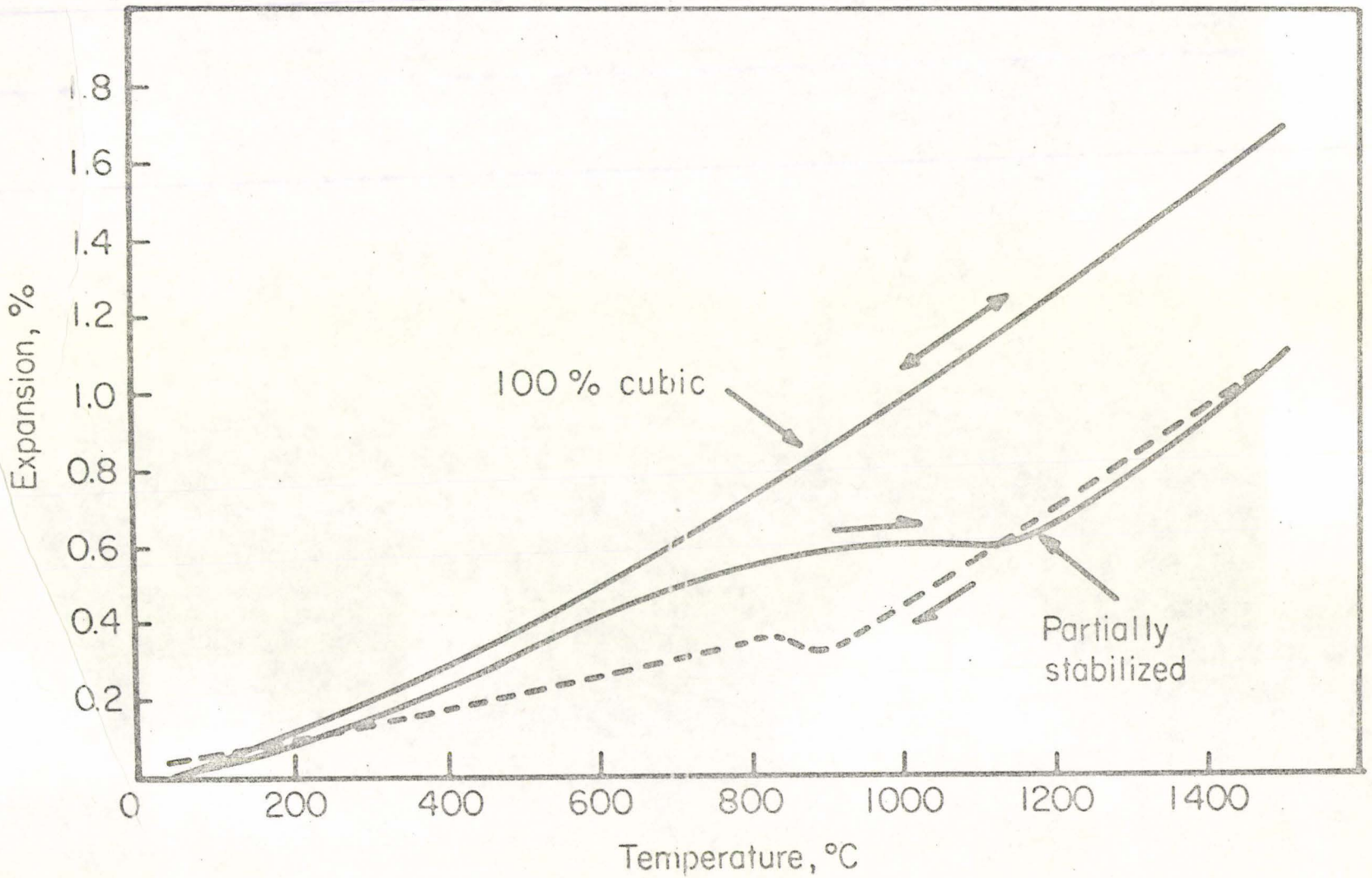

Figure 20. Thermal Expansion of PSZ and 100% Cubic Zirconia. After Whittmore and Ault [112].

and their results are shown in Figure 21. An interesting aspect of these thermal expansion curves is that in both cases the phase transformation appears to start around 800°C instead of the expected 1050°C. Jaeger and Nickell [107] concluded that the finely dispersed monoclinic phase may well be left in a stressed condition within the cubic matrix and it could be this internal stress which depresses the martensitic transformation temperature.

The destabilisation of cubic calcia-stabilised zirconia was mentioned previously to be small. This has been substantiated for calcia PSZ by Smoot and Whittemore [113], who found little or no destabilisation in PSZ made from pure oxides. Buckley and Wilson [114] did find substantial destabilisation in commercial calcia PSZ on thermal cycling but this could be due to the level of impurity in the commercial material.

These observations together with its reported high strengths [115] and the possibility of a stress-induced transformation could indicate the possible existence of a degree of toughness in this material. A study of the fracture process and the influence of the two-phase microstructure was therefore undertaken.

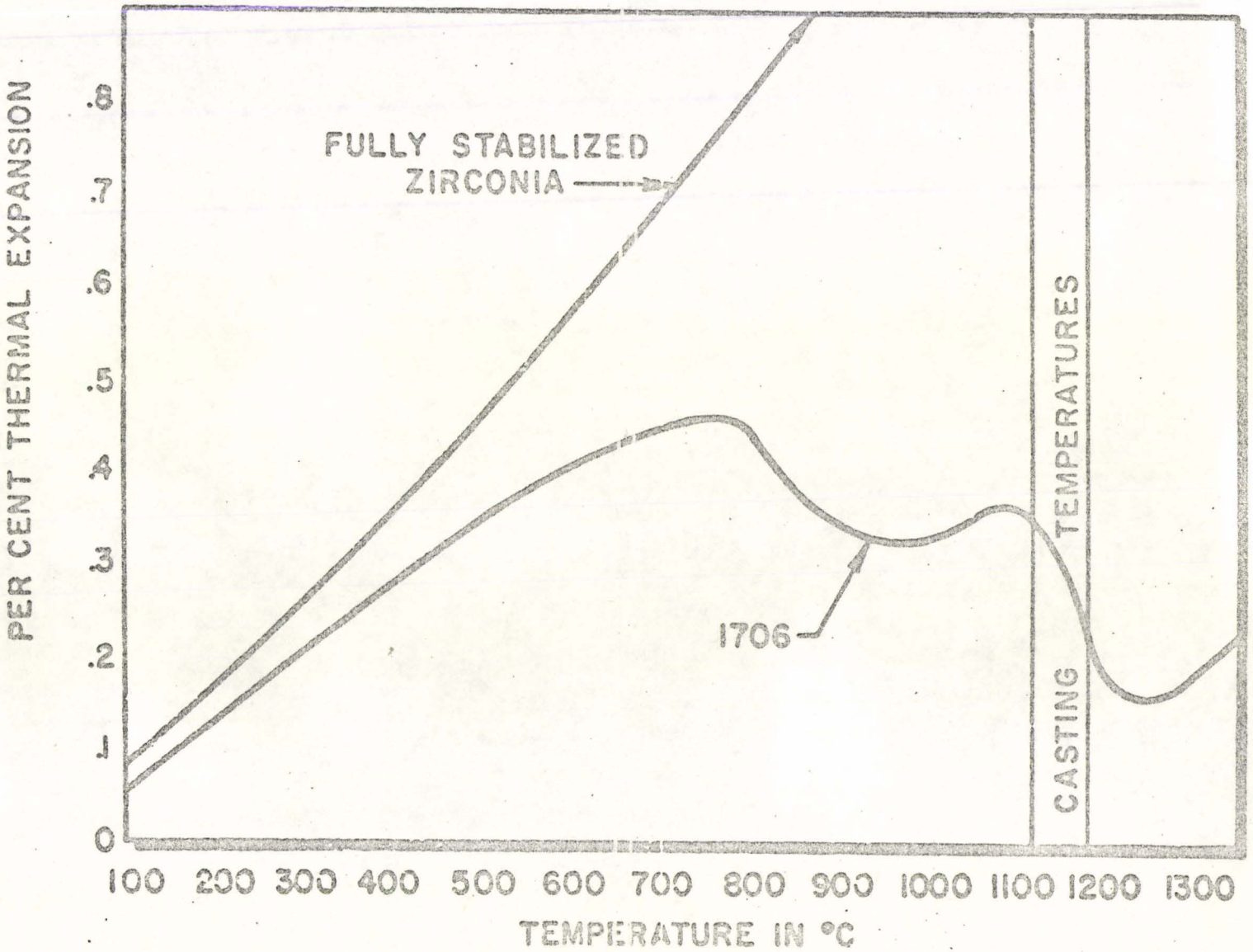

Figure 21. Thermal Expansion of Magnesia PSZ and 100% Cubic Zirconia. After Jaeger and Nickell [107].

CHAPTER II

EXPERIMENTAL PROCEDURE

2.1 Materials and Fabrication

Five different batches of calcia PSZ were received from Corning Glass Works and from Zircoa Limited. The first two batches from Corning Glass contained the same amount of calcia (3.4 wt.%) but were subjected to different heat treatments during fabrication. These two batches are designated batches 1 and 2. The other three batches from Zircoa were fabricated by similar techniques but with different levels of stabiliser (3.5, 3.8 and 4.5 wt.% CaO) and are designated batches A, B and C. As batches A, B and 2 proved to all intents and purposes to be identical, results of tests on batches 1, 2 and C only, will be reported.

The fabrication procedure consisted of cold-pressing the carefully mixed oxides into bars, using an organic binder. These bars were fired to 1750°C for several hours. The bars were then furnace-cooled to room temperature. The different heat treatments of batches 1 and 2 involved the rate of cooling after the firing stage. Batch 1 was slowly cooled to room temperature and batch 2 was fast-cooled.

The material received from Corning was in the form of 2 7/8 x 3/8 x 3/4 inch bars, and that from Zircoa was in the form of 2 1/2 x 3/8 x 7/16 inch bars.

Some of the batch 2 material was re-fired to 1700°C for five hours and then slow-cooled to room temperature at approximately 150°C/hour. This

material is designated #2 (annealed).

2.2 Preliminary Tests

The as-received materials were tested to determine some of their basic properties.

2.2.1 Density

The apparent densities of the five batches of calcia PSZ were determined by a water displacement technique.

The sample was suspended on a balance and weighed. The sample was then placed in a beaker of distilled water and boiled for a few minutes to remove any entrapped air and to allow the water to penetrate as far as possible into the sample. The weight of the bar was then determined suspended in the water and from the weight of the sample and the volume of water displaced, the apparent density was determined.

The theoretical density of batch 2 material was determined by a pycnometric technique. The material was first ground and passed through a -325 mesh sieve (44 microns) to remove at least the intergranular porosity. The theoretical density was then determined using a clean, dry pycnometer (specific gravity bottle).

2.2.2 Unnotched Bend Strengths

The unnotched bend strengths were determined in four-point bending

using the apparatus shown schematically in Figure 22. The apparatus consisted of two, 2 1/2 inch diameter, recrystallised alumina rods attached to the load cell and crosshead of an Instron universal testing machine (Model TT-C). The knife edges were made of 1/4" diameter, high density alumina (Lucalox), set into grooves in the ends of the heavy alumina rods. The inner and outer spans of the knife edges were one and two inches respectively. The load cell was a standard tension-compression cell with a maximum range of 1000 lbs. The samples to be tested were polished on their upper and lower faces, to reduce the friction effects between the sample and the Lucalox knife edges. Friction due to the alignment pins was found to be negligible by following the movement of the cross-head with no sample present and no friction load was observed.

Six samples from each batch of material were fractured at a cross-head speed of 0.002 in/min. The sample size was 2 1/2 x 7/16 x 1/10 inches and they were machined from the as-received bars using a Micromatic precision wafering machine with a 1/16" diamond cutting wheel. The outer fibre stress (σ) and strain (ε) can be calculated using the elastic flexure formulae (Appendix 1):

$$\sigma = \frac{3PM}{BW^2} \qquad (2.1)$$

and

$$\varepsilon = \frac{3W\delta}{3ML-4M^2} \qquad (2.2)$$

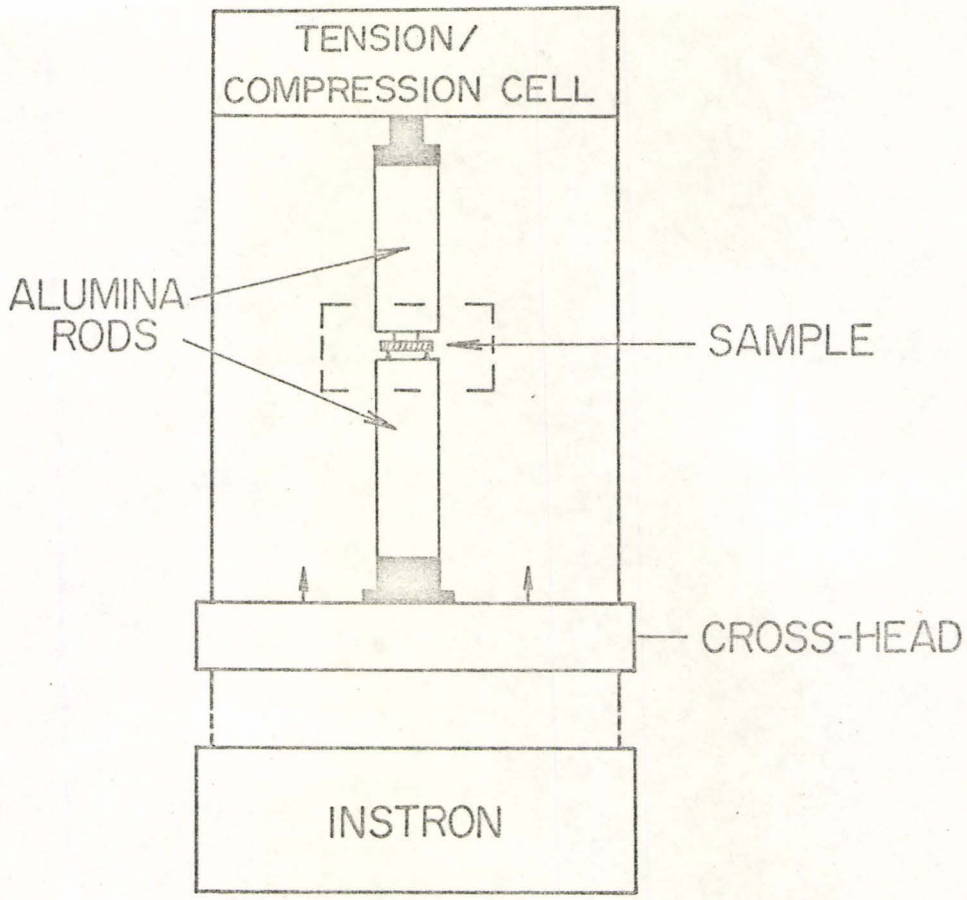

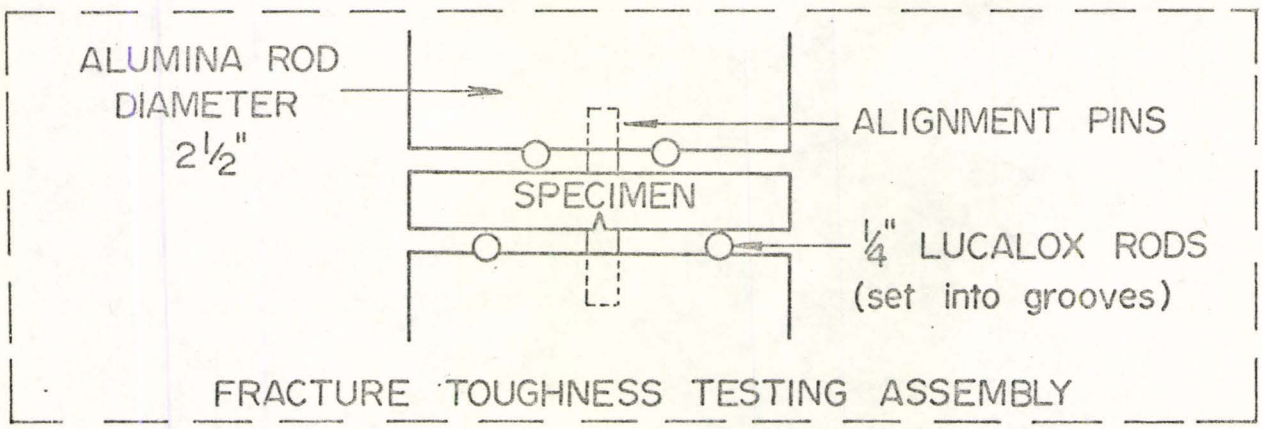

Figure 22. Schematic Diagram of Four Point Bend Apparatus.

where P = the applied load

M = the moment arm

B = specimen thickness

W = specimen depth

δ = deflection at the inner knife edges.

The fracture stress was determined from the maximum load values obtained. These tests would correspond to an outer fibre strain rate of approximately 0.14% per min, depending on the exact size of the sample.

2.2.3 X-Ray Diffraction

The different batches of calcia PSZ were ground to a fine powder (-325 mesh) and set onto microscopic slides using nail polish. These samples were placed in a Norelco X-ray diffractometer and were irradiated by CuK_α radiation using a graphite crystal monochromator. The samples were scanned in the range $2\theta = 25$ to 35°, at a scanning rate of $1/2^\circ$ 2θ/min. The monoclinic and cubic zirconia peaks were identified.

The integrated intensities were estimated, using a planimeter to measure the area under the diffraction peaks. The weight percentage of monoclinic zirconia was then estimated using the calibration of Garvie and Nicholson [129]:

$$\text{wt.\% monoclinic} = \frac{I_m(111) + I_m(11\bar{1})}{I_m(111)+I_m(11\bar{1})+I_c(111)} \qquad (2.3)$$

where $I_m(111)$ = integrated intensity of monoclinic {111}

$I_m(11\bar{1})$ = integrated intensity of monoclinic $(11\bar{1})$

$I_c(111)$ = integrated intensity of cubic {111}

2.2.4 Chemical Analysis

Chemical analysis was carried out on the received batches of calcia PSZ to determine the amount of calcia present.

The samples were ground to a fine powder and fused with lithium metaborate, $LiBO_2$, at 1000°C. The mixture was then quenched in distilled water and dissolved using concentrated hydrochloric acid HCl. This solution was then analysed for calcium using the atomic absorption spectrophotometric technique (Perkin Elmer Model 303).

2.3 Fracture Energy Measurements

The effective surface energy and work to fracture data was obtained from the load-deflection characteristics of notched samples of batches 2 and C. The apparatus was identical to the four-point bend apparatus used to measure the unnotched bend strengths. Similar steps were taken to reduce the friction effects between the sample and the loading points.

2.3.1 Specimen Dimensions and Test Geometry

There are several considerations to observe when choosing the sample for a plane-strain fracture toughness test.

The accuracy with which the critical stress intensity K_{IC} describes the fracture behaviour, will depend on how well the stress intensity factor represents the stress and strain within the fracture process zone. This will only truly occur in the limit of zero plastic strain. For practical purposes a sufficient degree of accuracy can be obtained if the crack front plastic zone is small in comparison with the vicinity around the crack, in which the K_I values yield a satisfactory approximation of the exact elastic stress distribution. Brown and Srawley [4] have outlined a procedure to make sure that crack length, specimen thickness and ligament size do not produce unsatisfactory errors in this respect.

In general for ceramics, the deviation from elastic linearity is negligible at ambient temperatures and the plastic zone effects are not important. However, it will be shown that for batch 2 such a deviation exists and is caused by a microcrack zone. There is no set procedure for correcting for such an effect but since the deviation was only small at the crack lengths used, the effect was disregarded. There are, however, other considerations to be observed in a four-point bend test.

Four-point bending produces pure bending inside the minor span and the calibration for stress intensity need therefore take no account of shear stresses, provided the ratio of the minor span to specimen depth (W) is not less than two. This is based on the fact that part of the strain energy field that is appreciably affected by the crack length, extends a distance W on either side of the crack [35]. Furthermore, to avoid specimen indentation and friction at the supports, the major support span should be at least four times greater than the specimen depth [35].

For the above reasons, a sample size of 2 1/2 x 7/16 x 1/10 inches was chosen, with major and minor spans of two and one inches respectively. The sample size and loading arrangements allowed all three techniques for the evaluation of the fracture surface energy to be taken from each set of data.

2.3.2 Notch Production

The notches were introduced into the samples by an ultrasonic technique, using a boron carbide slurry and a vibrating mild steel tool to grind a fine notch into the specimens. The depth of the notch was measured with a travelling microscope but since the notching technique produces an area of damage at the notch tip, the size of the observed inherent flaws was added to this value.

This method allowed notches with tip radii of 0.005 inches to be produced, an example of which is shown in Figure 23. It is hoped that this technique allows production of an array of independent microcracks at the crack tip, consistent with sharp-crack fracture mechanics. Dye penetration tests were used in an effort to define the notch depth using Dubl. Chek. DP-50 dye penetrant (Sherwin Inc.). This approach, however, proved unsuccessful for the batch 2 material since the material readily absorbed the dye, with or without notches.

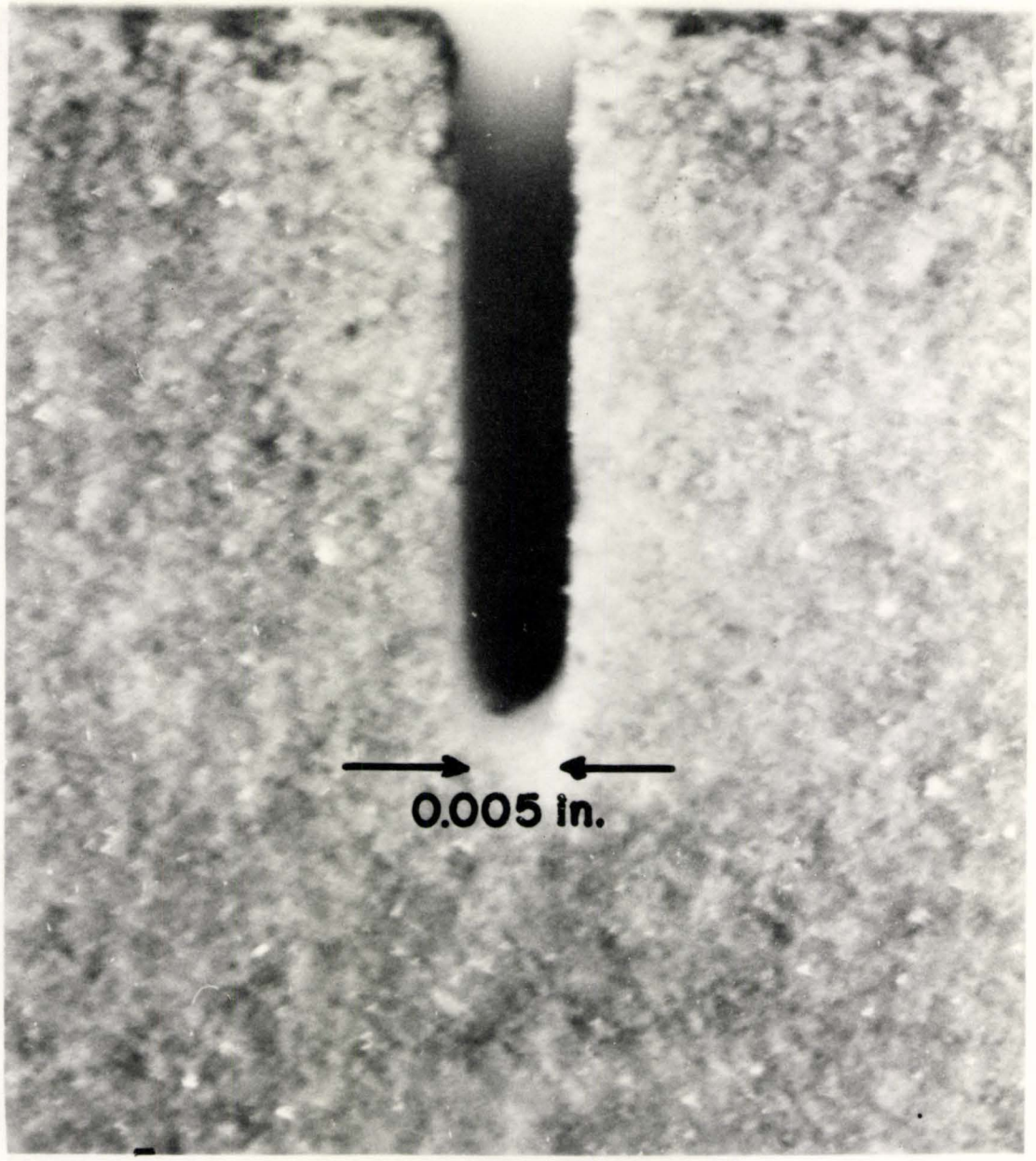

Figure 23. Ultrasonically drilled notch.

2.3.3 Stress Intensity Calibration

2.3.3.1 Stress Analysis

The stress intensity calibration was carried out by Gross and Srawley [68] for pure bending and has been extended to cover larger notch depths by Srawley and Brown [4]. This calibration can be applied to four-point bending since pure bending exists within the minor span.

The point of instability for the tests on calcia PSZ was taken as the maximum load value and the crack length at this point was taken as the initial notch depth. The critical stress intensity can then be calculated using:

$$K_{IC} = \sigma_F Y a^{1/2} \qquad (2.4)$$

where the fracture stress, σ_F, is given by (2.1) and the geometric factor is calculated using (1.24). The effective surface energy can then be determined from:

$$K_{IC}^2 = 2E\gamma_I \qquad (2.5)$$

The computer program for the effective surface energy calculation is included as Appendix 2. The calibration was carried out for a series of notch depths at a cross-head speed of 0.002 inches/min and a series of strain rates at a constant notch depth to specimen depth (W) of 0.2. Six samples were fractured at each notch depth and strain rate. In theory,

the observation of stable cracking in the batch 2 material would allow the fracture resistance to be determined as a function of crack length within a given test. The difficulty of measuring the dynamic crack length, however, made this approach very difficult. Stable crack propagation was utilised to observe the load-deflection characteristics for samples which had been unloaded after partial crack propagation.

Similarly, load-unload tests were also carried out using a 1/2 inch Instron strain gauge extensometer (Model G57-11) attached to symmetrical grips on either side of the notch. The extensometer attachment on a bar is shown in Figure 24.

2.3.3.2 Compliance Analysis

The compliance technique was also applied to the load-deflection data from the samples fractured from different initial notch depths. From a knowledge of the sample stiffness as a function of initial crack area and the deflection of the sample at fracture, the effective surface energy can be calculated using (1.28). The accuracy of this determination was not very good since deflections were small and based only on the cross-head movement. It was hoped, however, that this procedure could serve as a check on the previous stress analysis calibration.

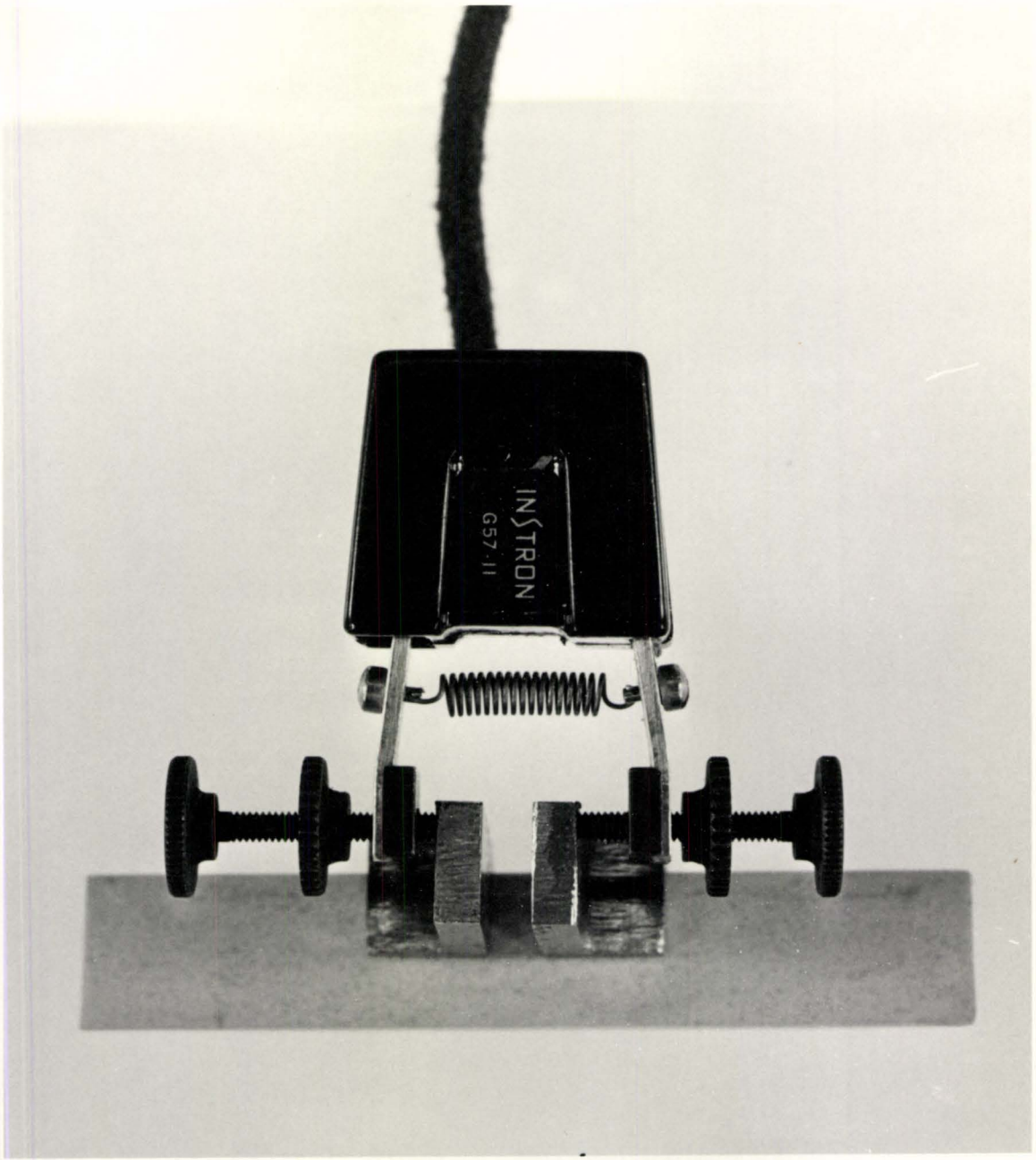

Figure 24. Extensometer Attachment to Sample.

2.3.4 Work to Fracture

This technique requires the use of a stiff loading system and the production of stable cracking. Stable crack propagation was readily available in batch 2 but was never observed in batch C and these latter results should therefore be viewed with caution.

The total work done in the fracture process (V) is associated with the area under the load-deflection curve and this was measured using a planimeter. The work to fracture (γ_F) can then be calculated since:

$$\gamma_F = \frac{V}{2BW} \qquad (2.6)$$

The work to fracture was calculated for different notch depths and strain-rates; six samples were fractured for each value. Since this technique is known to be sensitive to the loading arrangement, tests were also carried out at notch depth to specimen width of 0.2 using a harder load cell. This load cell was again a standard Instron tension/compression cell with a maximum range of 10,000 lbs.

The use of a special notch to induce stable fracture was not employed since the batch 2 material exhibited slow, stable crack growth.

The results for all these fracture energy measurements are quoted with errors that are the standard deviations associated with the result distribution. The experimental errors are estimated in Appendix 3, where it is shown that they are much smaller than those associated with the random nature of the fracture process.

2.3.5 Young's Modulus Determinations

Since it is necessary to use the value of Young's modulus when converting stress intensity to an effective surface energy, it was determined by three different techniques.

The value of Young's modulus (E) can be determined from the speed of stress waves in a material. The longitudinal wave velocity (C_l) in an infinite, isotropic body is given by [121]:

$$C_l = \sqrt{\frac{K + 4/3\ \mu}{\rho}} \qquad (2.7)$$

where K is the bulk modulus, μ is the shear modulus and ρ is the density of the material. The elastic constants can both be related to Young's modulus if Poisson's ratio is known.

Samples of batches 2 and C were polished to promote contact with the transmitter. The transmitter/receivers were 1/4 inch S.C.J. type crystals with frequencies of 2 1/4 and 10 MHz. The transmitted and reflected pulses were monitored on a Sperry UM775 Reflectoscope, which had been calibrated with a Tektonic 549 oscilloscope.

The Young's modulus can also be determined from the bend tests using the elastic flexure formula (Appendix I):

$$E = \frac{PL^3}{8\ \delta\ BW^3} \qquad (2.8)$$

where P = applied load, L = major support span, δ = deflection at inner

supports, B = specimen thickness, and W = specimen depth.

These elastic formulae are based on idealised elastic beam theory and the load and deflections should be accurately determined.

Finally, compression tests were performed on 7/16 x 1/4 x 1/4 inch rectangular samples using the Instron universal testing machine (Model TT-C) with a standard compression load cell (maximum range of 10,000 lbs). The strain was measured using an Instron strain gauge extensometer (Model G57-11) and the experimental set-up is shown in Figure 25. The modulus can then be easily determined from the slope of the stress-strain curves.

This experimental design also allowed the compression load-unload characteristics to be studied, and these tests were also performed on both the batch 2 and C materials.

2.4 Electron Microscopy

2.4.1 Scanning Electron Microscope (S.E.M.)

Fracture surfaces of the different batches of calcia PSZ were studied in the scanning electron microscope.

Sections of the fracture surface were cut from the notched bend specimens with a diamond cutter and mounted on aluminum studs with conducting paint. The fracture surfaces were then coated with a thin evaporated film of aluminum and examined in a Cambridge Stereoscan scanning electron microscope.

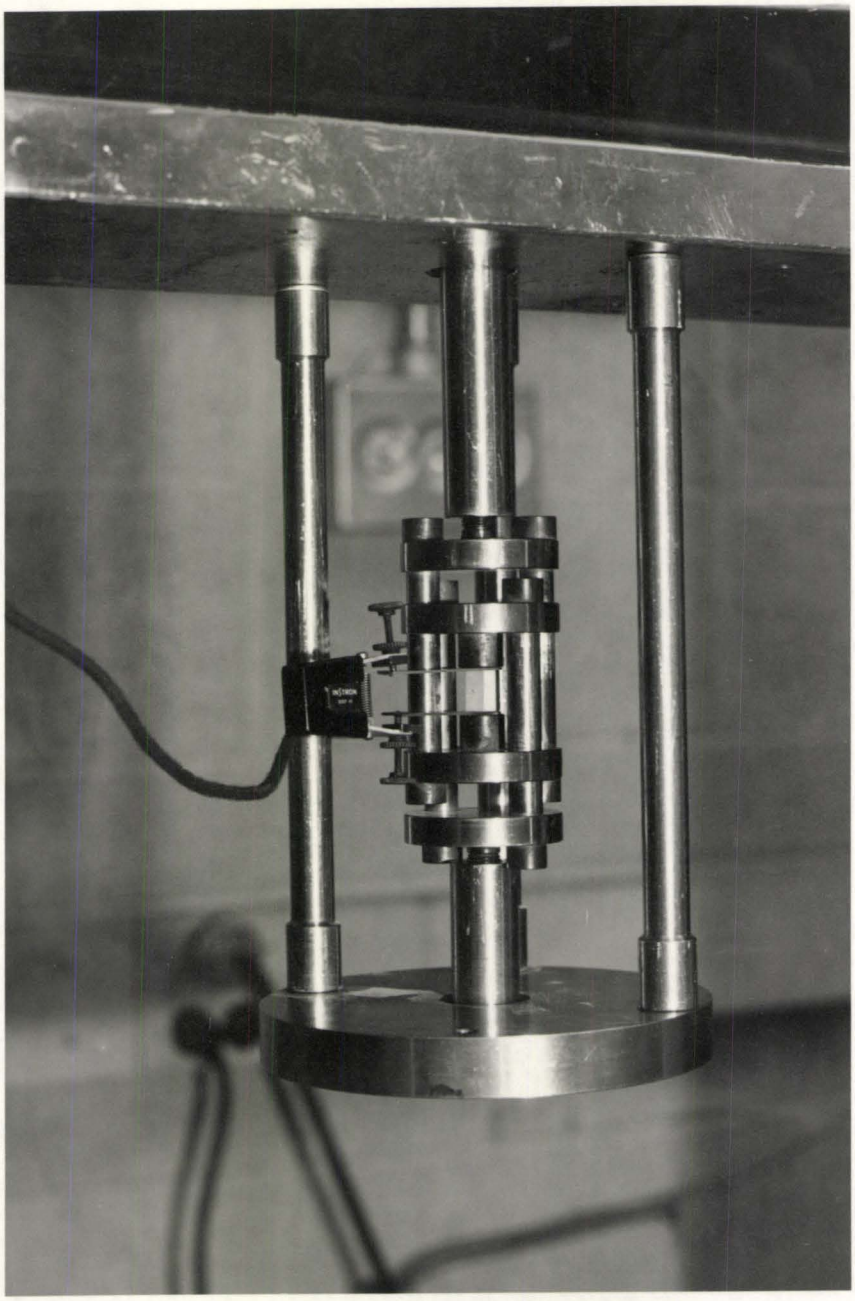

Figure 25. Experimental Arrangement for Compression Tests.

The morphology of the cracks was also studied, using samples which had been partially-broken and then vacuum-set in hard epoxy resin. These samples were polished on a series of emery papers to remove the surface resin and then on 6 and 1 micron diamond paste polishing wheels to produce a smooth surface. The apparatus for the vacuum impregnation of epoxy is shown in Figure 26. The sections containing the crack were cut from the specimen using a diamond cutter, attached to the aluminum studs with conducting paint and coated with a thin film of aluminum. These samples were also studied with the S.E.M.

2.4.2 X-Ray Analysis

A Nuclear Diodes Edax X-ray analyser was used in conjunction with the scanning electron microscope to obtain qualitative information on the composition of the phases observed at the fracture surfaces.

2.4.3 Transmission Electron Microscope (T.E.M.)

Two-stage, T.E.M. replicas were studied using a Philips EM300 transmission electron microscope. These replicas were taken from areas near the main crack to observe any secondary cracking processes.

The plastic solution was allowed to set on the polished specimen surface and was then carefully peeled off. The plastic stage was coated with carbon and the plastic dissolved away using an organic solvent. The carbon stage was then carefully placed on an electron microscope grid and studied in the transmission electron microscope.

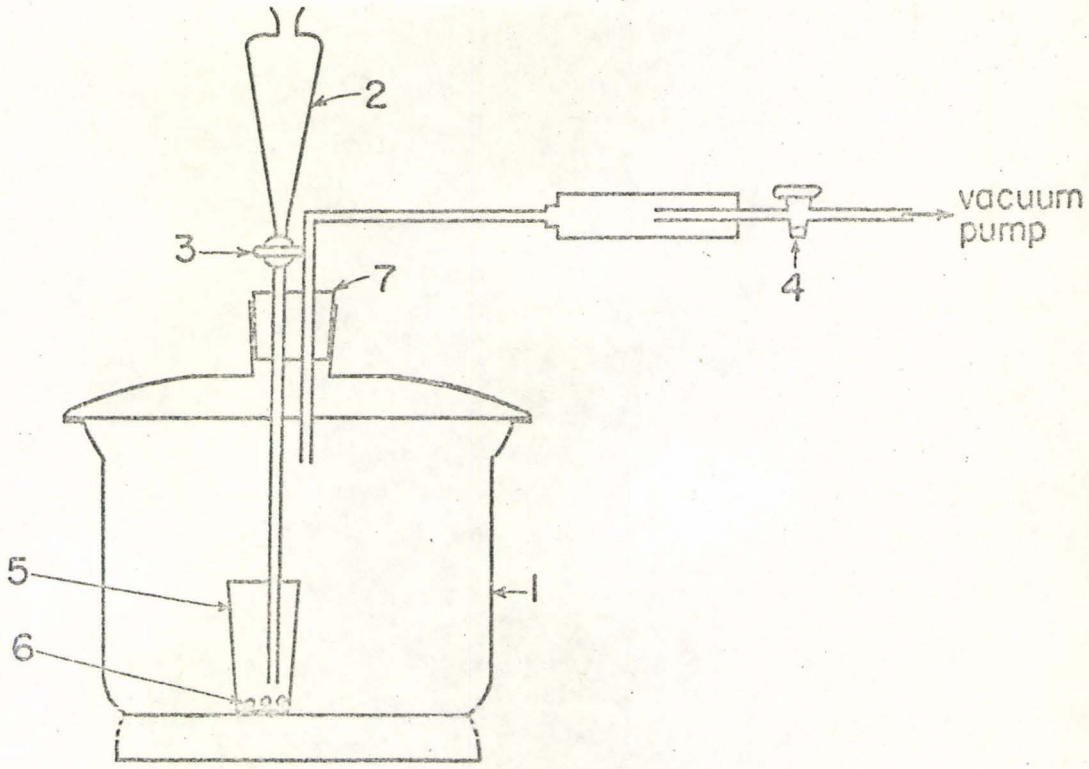

Figure 26. The impregnation assembly.

1. Desicator
2. Separating funnel with a long end
3. One-way stopcock to let in epoxy resin with hardener
4. One-way stopcock to connect or isolate the vacuum pump
5. Paper container
6. Samples
7. Rubber stopper with 2 holes

2.5 Thermal Expansion Tests

The thermal expansion of batches 1, 2 and C were measured to determine the temperature at which the martensitic transformation starts in these materials. The increase of specimen length was measured as a function of temperature using the standard British Ceramic Society specified dilatometer (F. Malkin and Co. Ltd.). The increase in length was measured using a dial guage and a Pt-13% Pt/Rh thermocouple was used to measure the temperature.

2.6 Quench Tests

In order to obtain some information on the thermal shock resistance of calcia PSZ, quench tests were performed on batches C and 2 (annealed).

Samples were cut from the fractured bars used in the fracture toughness tests, of dimensions 1 1/8 x 1/10 x 3/16 inch.

The specimens were placed in a furnace at temperatures up to 1150^{o}C and were allowed to soak at least two hours. The samples were then quenched to room temperature into a large beaker of water. After quenching, the samples were dried overnight in a furnace at 100^{o}C and then slowly cooled back to room temperature.

The strengths of the bars were then determined from three-point bend tests using the apparatus shown in Figure 22, but with the outer knife edges removed and replaced by one central knife edge (Lucalox). Six samples were fractured for each quenching temperature.

CHAPTER III

RESULTS AND DISCUSSION

3.1 Development of the Microstructure

Before attempting to discuss the fracture properties of calcia PSZ, it is important to define the microstructure, in order to understand their interdependence. This discussion will be limited, in general, to observations of the fracture surfaces in the S.E.M., for it is possible to gain a valuable insight by this method.

The preliminary definition of the five different batches of material is summarised in Table 3. The theoretical densities of calcia PSZ depend on the amount of calcia present. The decrease in density with increasing additions of calcia, is caused by the replacement of zirconium ions by lower atomic weight calcium ions, the increased vacancy concentration requisite to preserve electrical neutrality and the lower density of the stabilised cubic phase. Apparent density values are further complicated by the porosity left after fabrication.

The fracture stresses determined by four-point bend tests are also listed in Table 3. These strengths and the form of the stress-strain response (Figure 27) exhibit extremely varied behaviour. The fast-cooled batch 2 material shows low strength and stable crack propagation, while the high-calcia composition, batch C, shows high strength and unstable,

TABLE 3

Preliminary Tests on the Various Batches of Calcia PSZ

Batch	Density	Nature of Crack Propagation	Fracture Stress (ksi)	Wt.% CaO	Wt.% Monoclinic
#1	5.49	semi-stable	(5.0)*	3.4	40%
#2	5.76	stable	2.3	3.4	27%
A (Zircoa)	5.46	semi-stable	4.4	3.5	30%
B (Zircoa)	5.52	semi-stable	4.8	3.8	12%
C (Zircoa)	5.44	unstable	17.8	4.5	<7%
#2 (annealed)	5.75	semi-stable	5.0	3.4	27%
Powder #2	5.79			3.4	27%

* estimated

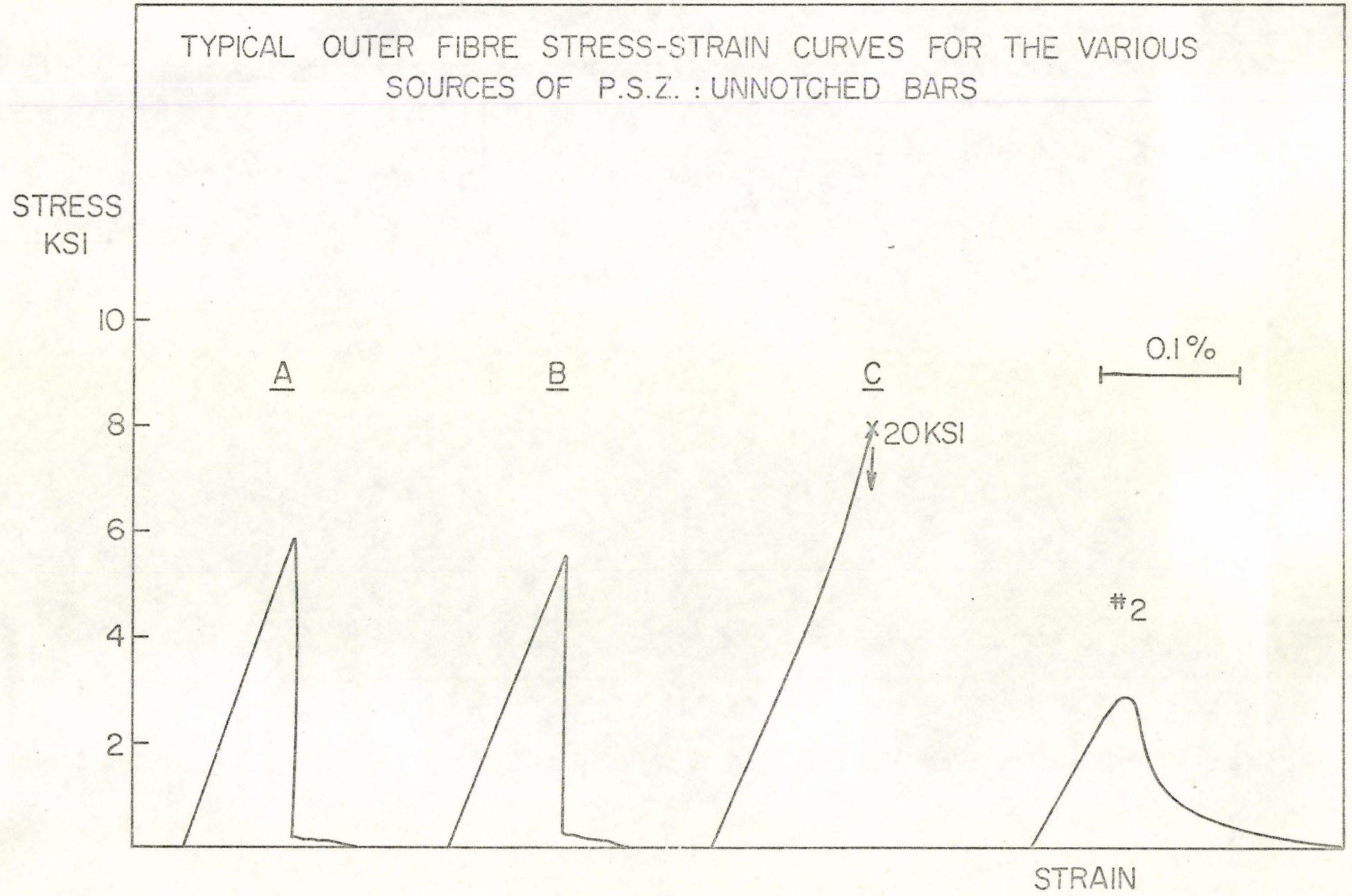
TYPICAL OUTER FIBRE STRESS-STRAIN CURVES FOR THE VARIOUS SOURCES OF P.S.Z. : UNNOTCHED BARS
STRESS KSI
10
8
6
4
2
A
B
C
0.1%
20KSI
#2
STRAIN

Figure 27.

catastrophic crack propagation.

The fracture surfaces of the different materials investigated are shown in Figures 28 - 33. The fractographs of batches 1 and 2 (Figure 28) show the structure to be bimodal in both cases, i.e., the structure consists of two regimes of grain size, with the smaller grains located on the grain boundaries of the larger grains. Fracture of batch 1 shows a mixed mode with the large grains failing transgranularly and the small grains intergranularly. Batches A, B and 2, however, exhibited completely intergranular fracture and the bimodal structure is clearly revealed. The high strength batch C material, a fractograph of which is shown in Figure 30, failed transgranularly and very little grain boundary phase is evident. Composite fractographs of batches 1 and 2 were made to show the fracture surfaces of these materials in greater detail and are included as Figures 31 and 32. The difference in fracture behaviour of these different batches is thought to be caused by the nature of the grain boundary phase, which will be discussed later in this section. The material designated #2 (annealed) was the fast-cooled batch 2 material, re-fired to 1700^{o}C and slowly cooled. Following this treatment, the strength was more than doubled and was comparable to that of batch 1. The fracture surface of this annealed material, Figure 33, is also similar to that of batch 1. The grain sizes of the different batches of material were determined and are included in Table 4.

As outlined previously in the experimental procedure, the fabrication of the material consisted of firing the carefully mixed oxides into the single-phase cubic region of the phase diagram, Figure 16. On

FRACTOGRAPHS SHOWING DIFFERENCE IN FRACTURE MODE BETWEEN BATCHES 1 and 2.

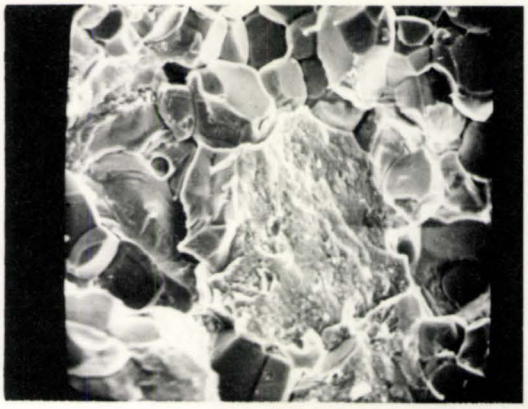

BATCH ONE

30 μM

BATCH TWO

10 μM

Figure 28.

FRACTOGRAPHS - ZIRCOA A and B.

A

B

56 μM

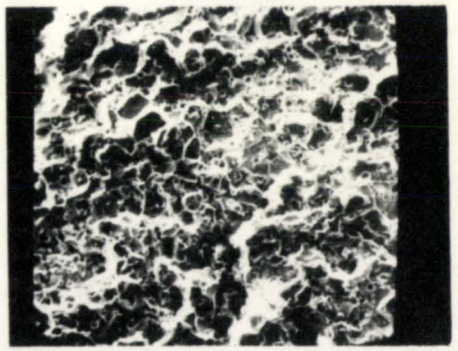

55 μM

25 μM

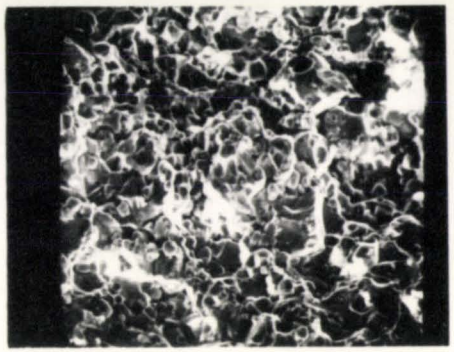

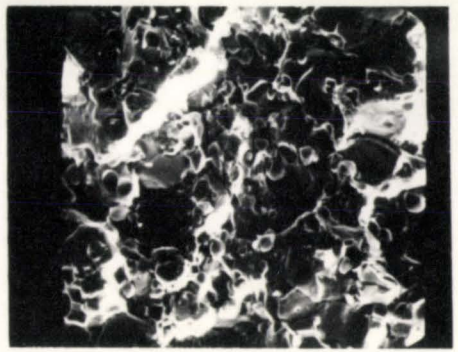

22 μM

Figure 29.

FRACTOGRAPHS OF BATCH C (HIGH STRENGTH P.S.Z.)

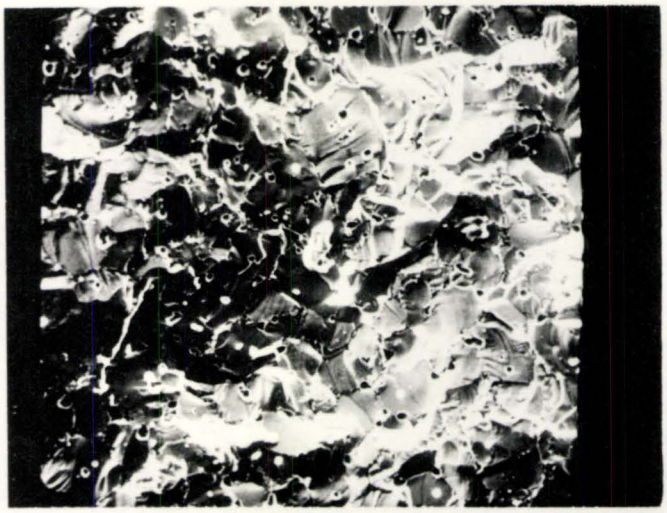

60 μM

20 μM

Figure 30.

COMPOSITE OF FRACTURE SURFACE : FIRST BATCH OF MATERIAL.

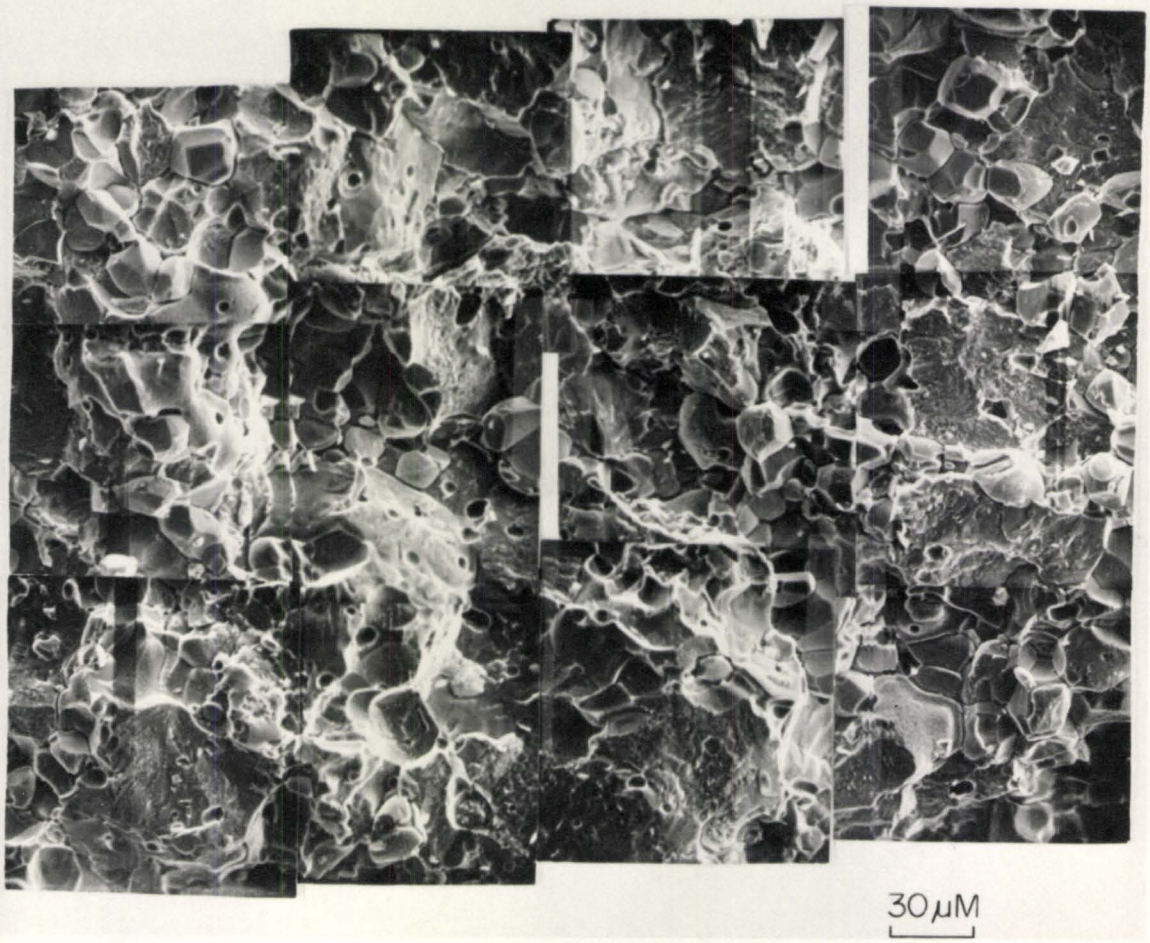

Figure 31.

COMPOSITE PHOTOGRAPH OF P.S.Z. FRACTURE SURFACE AT ROOM TEMPERATURE (DEFLECTION RATE .002"/min.)

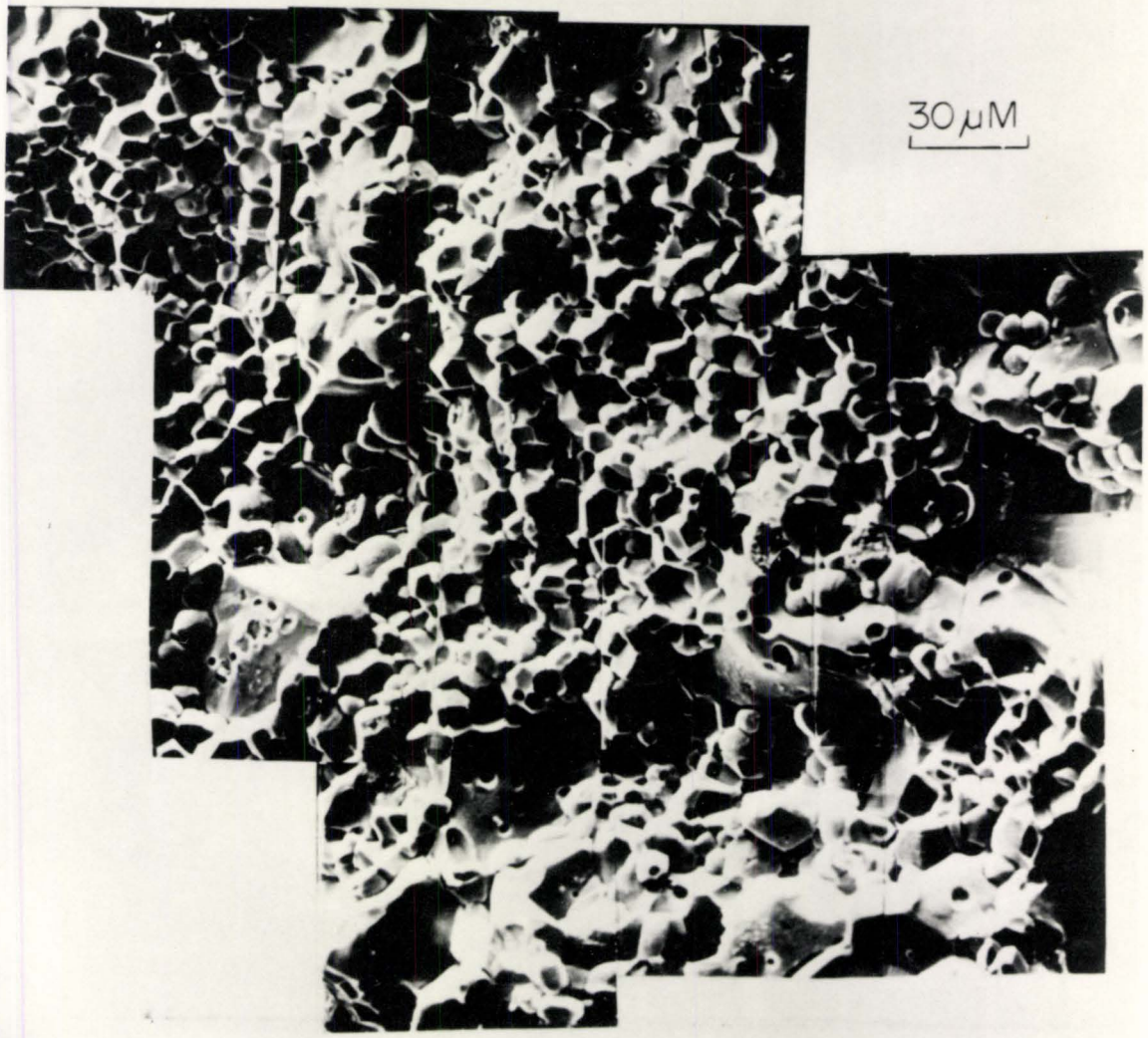

Figure 32

Batch #2.

FRACTOGRAPH OF BATCH 2
AFTER 1700°C ANNEAL

25 μM

Figure 33.

TABLE 4

Grain Size of the Batches of Calcia PSZ Taken From the Fractographs

Batch	Large	Small
A	60 μm*	8 μm
B	60 μm*	7 μm
C	50 μm	
1	80 μm*	20 μm
2	80 μm*	10 μm

* Some difficulty in estimation of these grain sizes because of the intergranular fracture features.

cooling, the cubic phase becomes super-saturated with pure zirconia, which should therefore precipitate out. This precipitation must involve either the diffusion of the calcium ions from the regions of pure zirconia, since the solid solubility limit of calcium ions in pure zirconia is very limited, or the diffusion of zirconium ions. The lattice self-diffusion coefficients for the cations in calcia stabilised zirconia have been determined by Rhodes and Carter [122] to be:

$$D_{Ca} = 0.444 \exp - (100,200/RT) \text{ cm}^2/\text{sec}$$

$$D_{Zr} = 0.035 \exp - (92,500/RT) \text{ cm}^2/\text{sec}$$

They also showed that these self-diffusion coefficients are not influenced by the oxygen vacancy concentration. These results should, therefore, hold for calcia PSZ. The precipitation of zirconia could be produced by the movement of calcium ions, which are the faster moving cation species. The oxygen diffusion coefficient in the material is relatively high. The ratio of 10^6 between the anion and cation diffusion coefficients is larger than observed in all other oxides except uranium dioxide. The cationic mobility is responsible for the slow rate of formation of cubic zirconia and for its low sintering rates. The high anion mobility gives it an electrical conductivity at 1000°C which is greater than the conductivities at the melting point of 13 of the 15 halides tabulated by Jost [123].

If, in precipitation of zirconia, only the calcium ions need to diffuse, then presumably they could either be precipitated as calcia or simply lead to an increase in the level of stabilisation of the remaining

cubic phase. It is thought that the latter process is most likely [124]. Rhodes and Carter [122] also noted that at temperatures around 1800°C the grain boundary diffusion coefficient of calcium ions is approximately 10^5 times the lattice self-diffusion coefficient. Therefore, at the grain boundaries where nucleation is relatively easy and where the diffusion coefficient of calcium is high, the pure zirconia should be precipitated first. This idea would suggest that the smaller grained material present at the grain boundaries could be pure monoclinic zirconia.

X-ray analysis for calcium Kα peaks was carried out on the S.E.M. and the results are shown in Figure 34. The results show that the amount of calcium present in the small grains is negligible compared with the large grains. Since the monoclinic zirconia has almost zero solid solution limit for calcia, the grain boundary phase is assumed to be pure monoclinic zirconia. There is a slight peak in evidence for the small grains but this could be caused by the calcium which may be present around the grain boundaries of the small grains. The accuracy of X-ray analysis on the S.E.M. is not yet fully understood but initial experiments have shown the electron spot size is not greater than 5 microns and it would seem reasonable to assume the X-ray information has just been produced from within these small grains. Concurrent X-ray analysis was also carried out on pure monoclinic zirconia powder and the results are also included in Figure 34. The presence of pure zirconia on the grain boundaries is also supported by the fact that the amount of the grain boundary phase decreases with increasing additions of calcia, i.e., as the level of supersaturation decreases. Attempts to produce a diffraction pattern for

Figure 34

X-RAY ANALYSIS FROM S.E. MICROSCOPE (3.0-5.5 KEV)

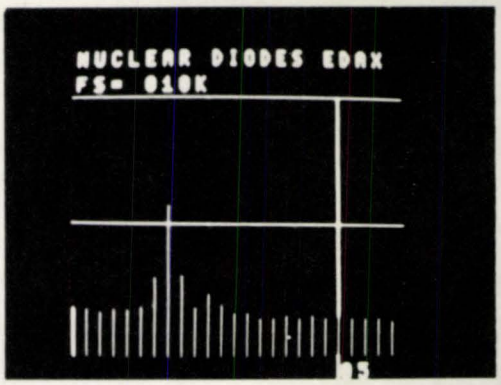

(A) LARGE GRAIN

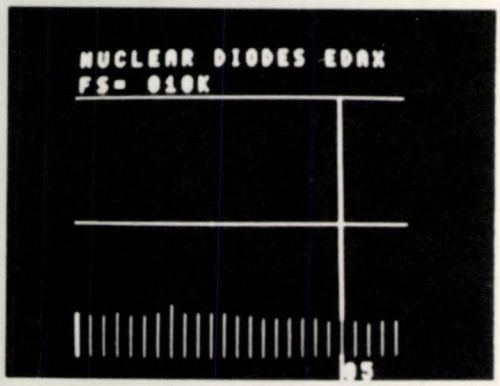

(B) SMALL GRAIN

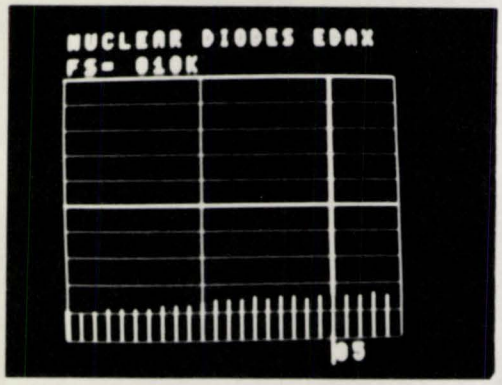

(C) MONOCLINIC ZrO_2 POWDER

the grain boundary phase were unsuccessful since the production of thin or polished sections invariably resulted in a loss of this phase during the abrasion processes involved.

There is evidence that the monoclinic phase is also present on a finer scale within the larger cubic grains. The electron micrograph of a two-stage replica, Figure 35, shows what may be a fine dispersion of a second phase within the large cubic grains. This idea is supported by the work of Garvie and Nicholson [6] and it would seem reasonable that at the lower cooling temperatures, where the lattice self-diffusion coefficient of calcium is low (approximately 10^{-15} cm^2/sec at 1200°C), that precipitation should occur on a much finer scale. This interpretation is also supported by the electron micrographs shown in Figure 36. These show the structure to be two-phase, with one phase heavily twinned. The observation of twinning in monoclinic zirconia [84,85] indicates that the twinned phase in the micrographs is probably the monoclinic phase. These observations are very similar to the microstructures of magnesia PSZ discussed in the literature review. The structure of this material, especially within the large grains, is very complex and has not been well-defined. However, for fracture in an intergranular mode, the internal structure of the large grains may only play a minor role. In materials such as batch I and the high strength batch C, where the grains do fail by cleavage, the finely dispersed phase should play a more important role. The internal structure of such a cleavage fracture is shown in Figure 37 and the existence of an internal grain structure is evident. It is thought, however, that the size and distribution of pure zirconia on the grain

Figure 35. Two-Stage Replica, Calcia PSZ (24,000 X).

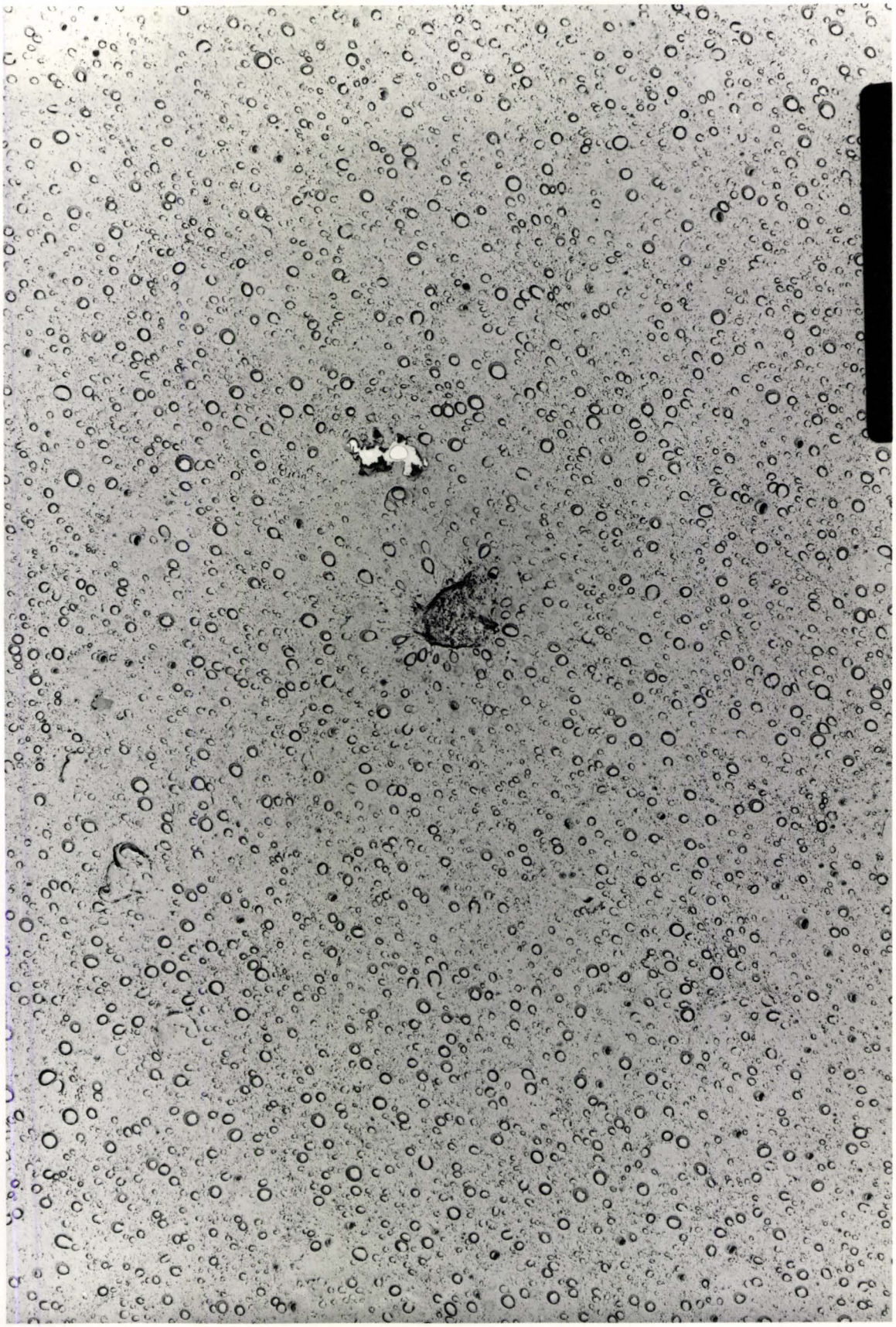

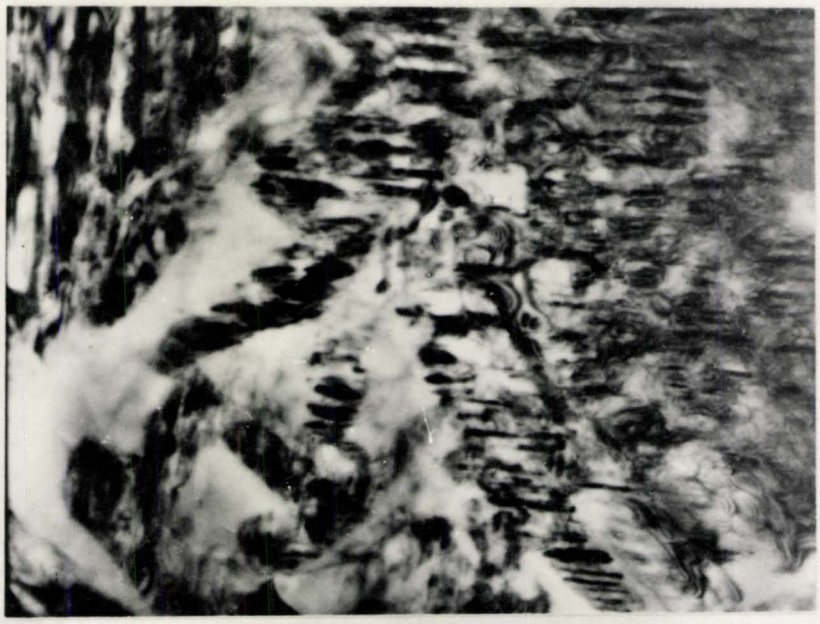

(C)

1.0 μm

(D)

0.5 μm

Figure 36. Electron Micrographs, Calcia PSZ.

TRANSCRYSTALLINE FRACTURE, BATCH ONE.

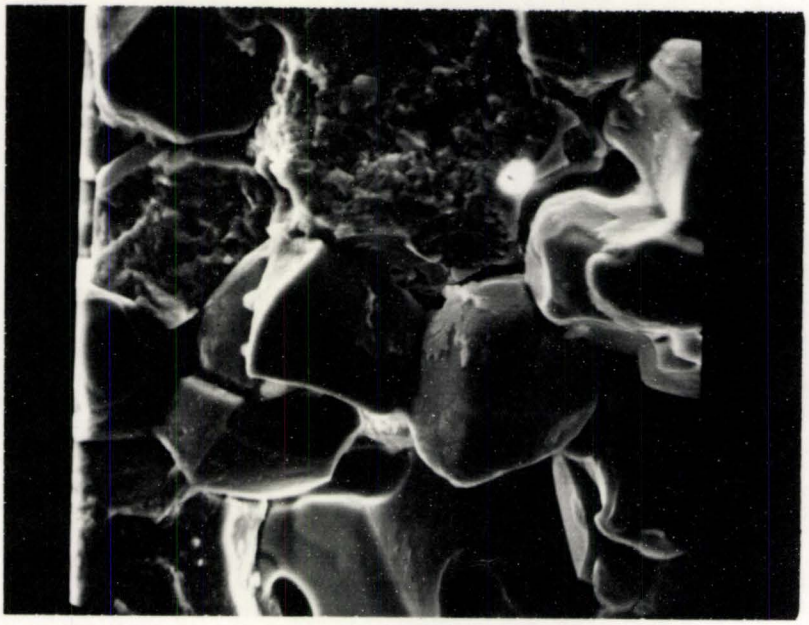

20μM

Figure 37.

boundaries is the major factor in the determination of the strength and fracture properties of the batches of calcia PSZ investigated.

The pure zirconia, precipitated on the grain boundaries, should be present initially as the tetragonal polymorph. At the later stages of cooling, the phase transformation to monoclinic will occur and this involves a 9 percent volume expansion. The transformation should give rise to large internal stresses within the body. The stress within the zirconia precipitate particles can be calculated approximately, using Selsing's equation [115]:

$$P = \frac{\Delta R/R}{(1+\nu_1/E_1) + (1-2\nu_2/E_2)} \qquad (3.1)$$

where R = radius of the inclusion

ΔR = misfit

E_1 and E_2 are the Young's modulus of the host and the inclusion, and

ν_1 and ν_2 are the Poisson's ratios of the host and the inclusion.

Assuming $\nu_1 = \nu_2 = 1/4$ and using the modulus values at 1000°C from the work of Wachtman and Lam, and Smith and Crandall [125,126], it is found that the internal stress $P \cong 100{,}000$ psi and the strain in the particle should be about 0.67%.

King and Yavorsky [106] proposed that slip would accommodate part of these stresses but the inability of the monoclinic phase to slip and the brittleness of the cubic phase make this mechanism seem doubtful except on a limited scale. It is proposed, therefore, that this strain is

more likely to be partially accommodated by twinning of the monoclinic phase and the formation of cracks, while the rest of the strain will remain as an elastic residual stress in the material.

The phase transformation, as just indicated, should produce an internal stress within the material. The stress in the precipitate particle was calculated but obviously the particles will also cause internal stresses within the matrix. The theory of elasticity shows that the shear strain at a distance r, from a particle of radius R with misfit ε_f should be:

$$\varepsilon_f R^3/r^3 \qquad (r < R) \tag{3.2}$$

Therefore changes in the state of dispersion without change in misfit alters only the "wavelength" of the stresses and not their "amplitude". The phase transformation should therefore produce some average internal stress in the material. If this internal stress, σ, can be taken as a simple average of the arithmetic magnitude of the stress (after Mott and Nabarro [127]):

$$\sigma = 2\mu\ \varepsilon_f f \tag{3.3}$$

where μ is the modulus of rigidity and f is the volume fraction of precipitate, then substituting the values obtained for the modulus of rigidity [128], the misfit strain calculated earlier and the volume fraction calculated from the X-ray diffraction scan using the calibration of Garvie and Nicholson [129], the average internal stress due to phase trans-

formation was calculated to be approximately 48,000 and 30,000 psi for batches 1 and 2 respectively. A typical X-ray diffraction scan is shown in Figure 38 and the weight percentage of monoclinic zirconia in the various batches of calcia PSZ are listed in Table 3.

The difference between batch 1 and 2 was the rate of cooling after sintering at 1750°C. The slow cool of batch 1 could allow the microstructure to approach equilibrium with respect to the amount of monoclinic zirconia. This is predicted to be 60% from the phase diagram. For batch 2 however, the fast cooling could restrict the amount of precipitation of pure zirconia and should accentuate any strain accommodation problems which arise from the phase transformation, particularly in the form of cracks. This idea is supported by the fact that when batch 2 was annealed at 1700°C and slow-cooled, the strength was more than doubled and the fracture surface appeared to be similar to that of the slow-cooled batch 1 material. This could indicate the occurrence of a crack-healing phenomena, where the higher density of cracks formed by the fast cooling are healed and the structure of the slow-cooled material is then reproduced. This idea is of practical importance since it shows that sometimes the thermal shock cracks produced in ceramics can be healed.

The evidence for the presence of microcracks in batch 2 is substantial. Dye penetration into the material was rapid and deep, as shown in Figure 39 and the small monoclinic grains tended to etch out when the material was polished. Furthermore, the small monoclinic grains fall out as debris from fracture surfaces. Figure 40 shows the fracture

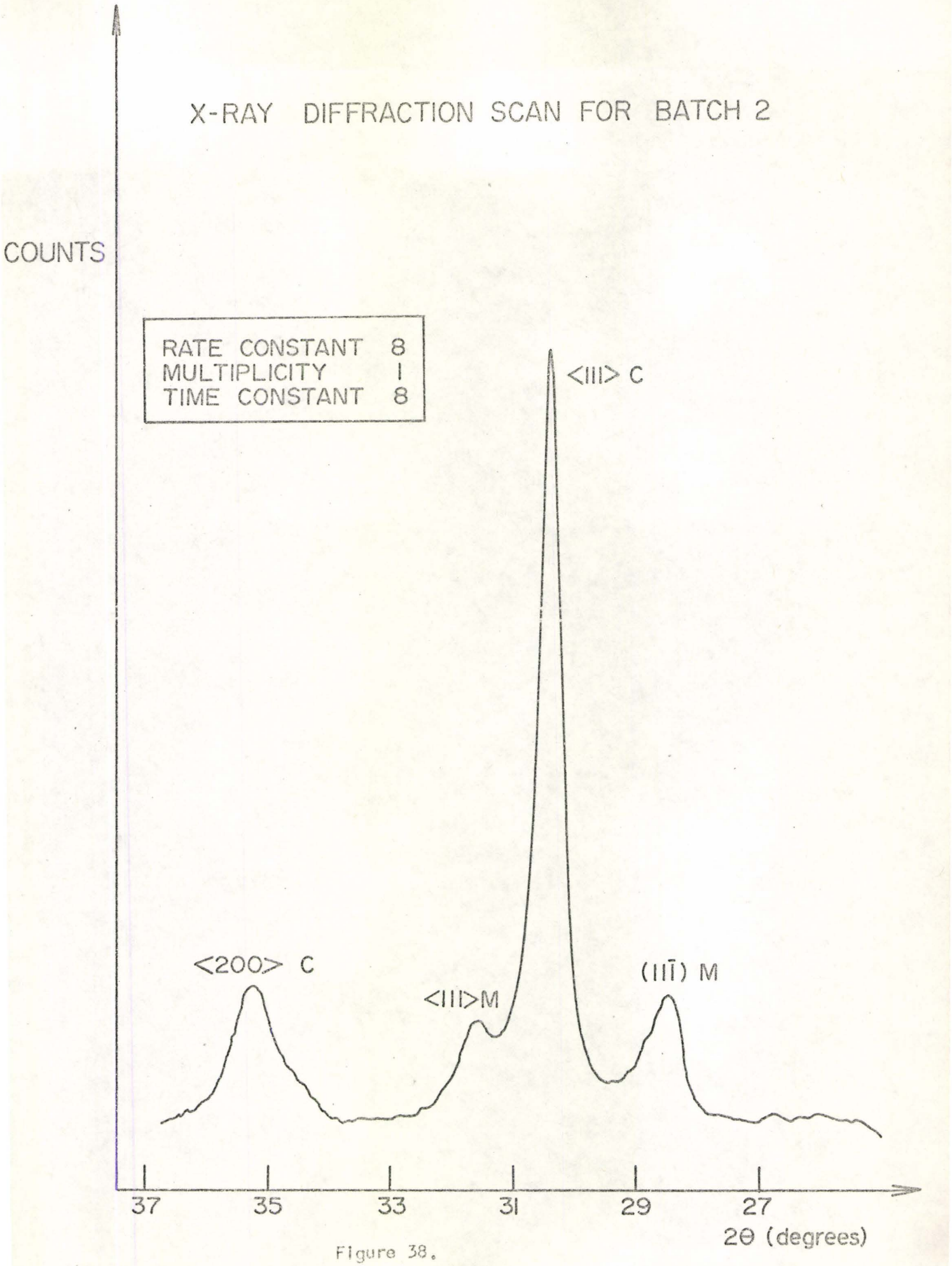
X-RAY DIFFRACTION SCAN FOR BATCH 2
COUNTS
RATE CONSTANT 8
MULTIPLICITY 1
TIME CONSTANT 8
<111> C
<200> C
<111>M
(11$\bar{1}$) M
37
35
33
31
29
27
2θ (degrees)

Figure 38.

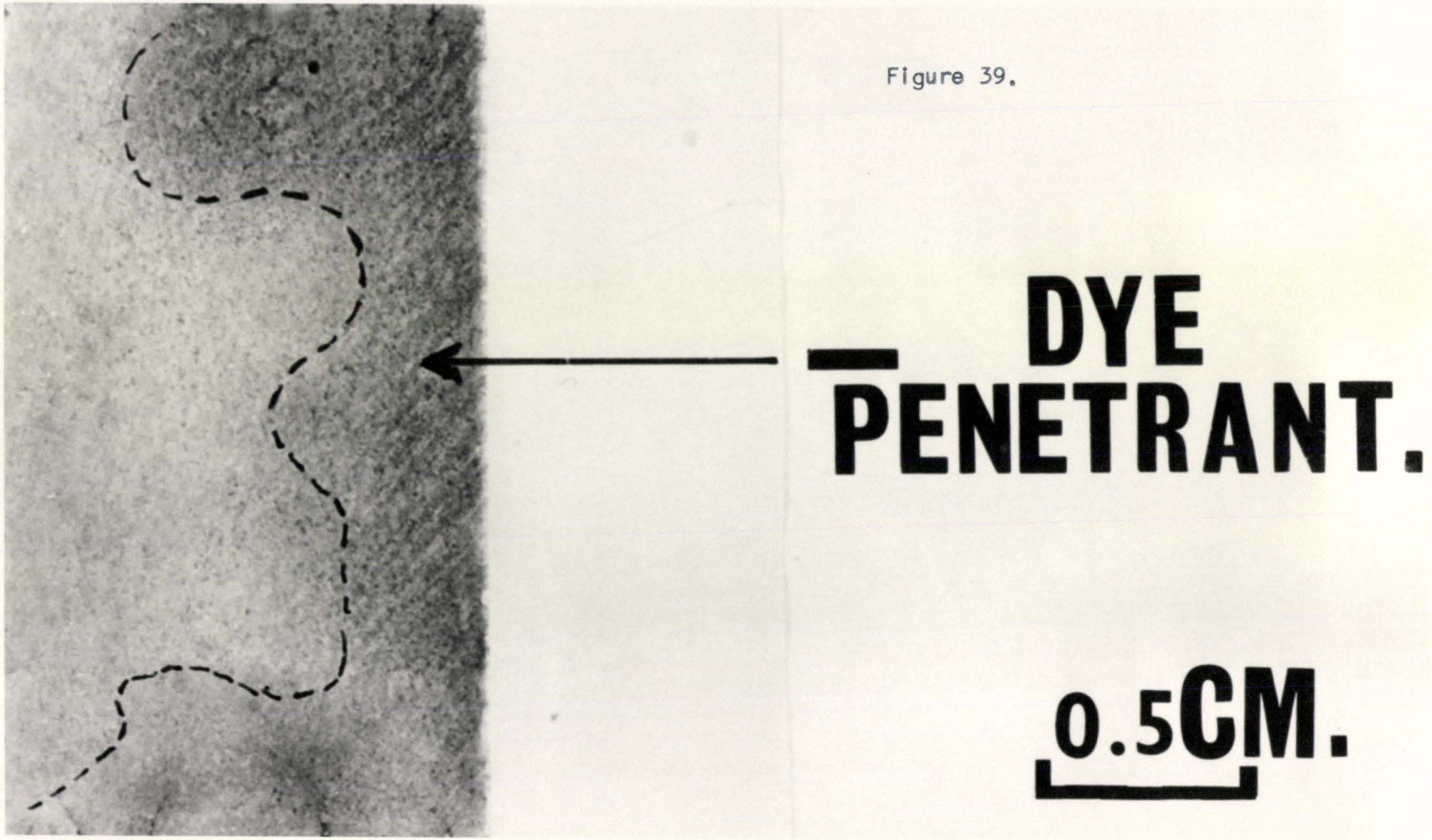

Figure 39.

SCANNING ELECTRON MICRO-GRAPH OF FRACTURE EDGE SHOWING TYPICAL DAMAGE AND LOOSE SMALL GRAINS.

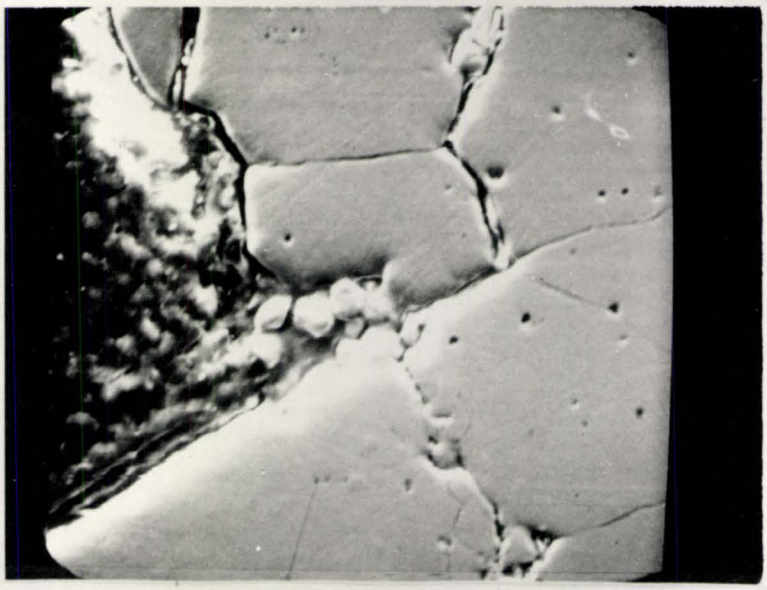

40 μM

Figure 40.

edge of a bar from batch 2, which has been set in hard epoxy resin after partial crack propagation. The loose monoclinic grains and the formation of cracks along the grain boundaries near the fracture surface are evident. The Young's modulus of batch 2 was determined by various techniques to be discussed in the next section. The values of the elastic modulus will be shown to be extremely low and this is consistent with the presence of microcracks in the batch 2 material. It is important to note, however, that the density of this material is very high, even with the presence of these cracks. Moreover, the material has been shown to be impermeable to oxygen gas since it can be used as an ionic conductor of oxygen ions. It was therefore deduced that the cracks must be extremely fine and are probably better considered as decohesed grain boundaries or fine two-dimensional microcracks.

It is proposed that these decohesed grain boundaries are formed by the internal stresses developed during the transformation. The expansion in the phase transformation will lead to compressive stresses within the monoclinic material, a tensile stress in the surrounding grains and a complex system of shear stresses across their interfaces. If the formation of the microcracks does not exhaust the internal stress, it will still tend to close the cracks and such a mechanism might account for their small volume. The ease of crack healing in the fast-cooled batch 2 material is also consistent with the idea of weak or decohesed grain boundaries. The mechanism of the decohesion is not clear but it is possible that the shear stresses involved in the martensitic phase transformation, acting at the surface of the monoclinic phase, may

produce the decohesion. Differences in the expansion coefficients of the two phases and the strain energy which is involved in the precipitation, may also play a role in the decohesive process but at temperatures above the phase transformation the tetragonal phase is quite ductile and these factors will probably not be important. It is thought, therefore, that it is the phase transformation which causes the decohesion. In contrast, the slow-cooled batch would be expected to have less decohesion and a larger residual stress at room temperature, since it contains a larger volume fraction of the monoclinic phase.

The work of Dow Whitney [92] indicates that the phase transformation is pressure sensitive. It follows therefore, that any internal stress on the monoclinic phase should be evidenced by a change in the temperature at which the phase transformation starts. Dilatometric experiments were undertaken on the material 1, 2 and C under constant rate of heating conditions. The resultant traces are shown in Figures 41, 42 and 43.

The form of the thermal expansion curves for batches 1 and 2 are complicated by the fact that while the cubic phase is expanding, the monoclinic phase is contracting due to the phase transformation. For batch 1, the transformation start is quite clear and this is probably due to the greater volume fraction of monoclinic present in this material. The start of transformation is harder to define in batch 2 and it was assumed to start where the thermal expansion curve changes slope. For both batches 1 and 2 the transformation is seen to start at a lower temperature than expected ($\sim 1000^{o}C$). This behaviour may be expected

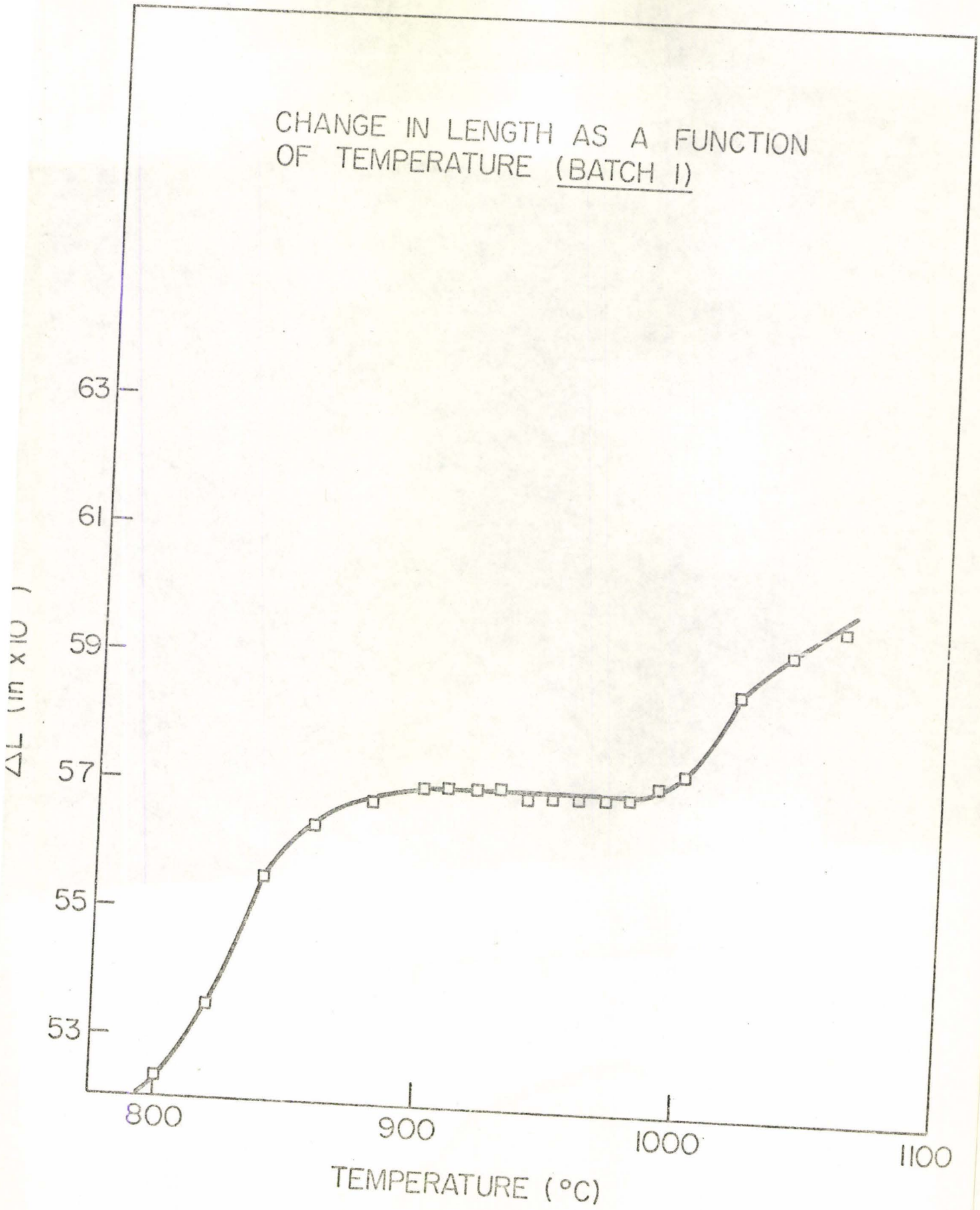
CHANGE IN LENGTH AS A FUNCTION OF TEMPERATURE (BATCH 1)
63
61
59
57
55
53
ΔL (in x 10)
800
900
1000
1100
TEMPERATURE (°C)

Figure 41.